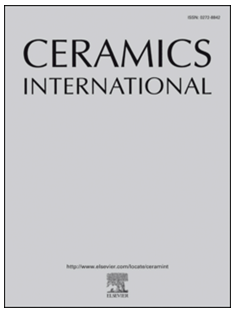

Physical and magnetic properties of $Ho_{1-x}Ba_xCrO_3$ ceramics

R. Triki Ben Youssef, Nasr Sdiri, M.A. Valente, K. Horchani-Naifer, M. Férid

PII: S0272-8842(19)31806-1

DOI: https://doi.org/10.1016/j.ceramint.2019.06.293

Reference: CERI 22102

To appear in: *Ceramics International*

Received Date: 19 April 2019

Revised Date: 25 June 2019

Accepted Date: 27 June 2019

Please cite this article as: R.T. Ben Youssef, N. Sdiri, M.A. Valente, K. Horchani-Naifer, M. Férid, Physical and magnetic properties of $Ho_{1-x}Ba_xCrO_3$ ceramics, *Ceramics International* (2019), doi: https://doi.org/10.1016/j.ceramint.2019.06.293.

Physical and magnetic properties of $Ho_{1-x}Ba_xCrO_3$ Ceramics

R. Triki Ben Youssef[a,b], Nasr Sdiri[a,*], M.A. Valente[c], K. Horchani-Naifer[a], M. Férid[a]

[a]Physical Chemistry Laboratory of Mineral Materials and Their Applications, National Center for Research in Materials Sciences, Technopark Borj Cedria, PO Box 73-8027 Soliman, Tunisia

[b]Faculty of Sciences of Bizerte, 7021 Jarzouna, Bizerte, Tunisia

[c]Department of Physics, I3N, University of Aveiro, 3810-193 Aveiro, Portugal

* Corresponding author.Tel : +21697480353.

E-mail address : sdirinasr@yahoo.fr(N.Sdiri)

Abstract

The set of $Ho_{1-x}Ba_xCrO_3$ with x= 0.0, 0.2, 0.3 was synthesized through sol – gel technique. Rietveld refinement of X-Ray Diffraction (XRD) patterns and Raman spectroscopy showed a single phase orthorhombic structure for all the samples. Raman analysis revealed the presence of the A_g phonon mode related to the existence of CrO_6 octahedra. Thermal studies were performed to show a thermal stability of the compounds. Pl measurements exhibited not only visible light emission but also intense NIR emission under excitation of UV light. Impedance spectroscopy indicated that DC conductivity can be explained by Arrhenius-type thermally activated process for x=0.0 and 0.2 whereas for x=0.3, it obeyed to Mott's law. The conduction mechanism was found to be referred to polaron hopping. The dielectric measurements revealed a polarization in the as-prepared samples with high values of dielectric constant and low dielectric loss in particular for x=0.3. Magnetic measurements

showed enhancement of magnetisation upon Ba substitution and the existence of a large magnetocaloric effect.

Keywords:Perovskite, Sol-gel process, Nanopowder, Magneto-caloric effect

1. Introduction

Perovskite rare-earth chromites with the general formula $RCrO_3$ comprise an important class of multiferoic materials [1-4] that exhibit an astonishing variety of physical properties including electric, dielectric, magnetic, magneto-caloric, optic properties and so on. As a result, in the past several years, they have been fully investigated due to the promising potentials of applications such as insultor-metal transition [5], fuel cells (SOFC) [6], magneto-caloric materials [7], oxygen sensors [8], dielectrics [9], optic-magneto devices [10].....

Several factors like the ionic size of the R^{3+} rare earth, the atomic valency of Cr- ions[11], Jahn Teller distortion [12] and the exchange between the d- orbitals of the B transition metal cation and the 2p-orbitals of oxygen anions [13-14] profoundly influence the electric, magnetic and other properties of these materials. Furthermore, these properties and the spin state of Cr ions can be controlled by a partial substitution either in R or/and Cr cation sites [13, 15, 16] which introduces a remarkable lattice distortion leading to various defects in the structure [17, 18]. The structural distortion plays a crucial role to explain several physical properties in these materials [12, 19-21]. So, these substitutions offer an exceptional research opportunity for condensed matter physics.

Among various chromium oxides, $HoCrO_3$ is the most fascinating compound that has attracted great attention due to its rich structural, magnetic and magneto-caloric properties[2,3,7,20,22], but to our knowledge, the crystalline structure and many physical phenomena are far from clearness. On the other hand, the possibility to improve the physical properties with a partial R-site ionic substitution has motivated us to study the mixed valence chromites$Ho_{1-x}Ba_xCrO_3$

To prepare these materials, a wide variety of chemical techniques has been developed such as solid-state reaction method [23], co-precipitation [24], hydro-thermal [25], the Pechini [26] and sol-gel progress [27]. In this paper, perovskite-type oxide $Ho_{1-x}Ba_xCrO_3$ was synthesized by sol-gel technique which is the simplest, most economical and less energy consuming route for nanoparticles synthesis.

The objective of this work is to present a detailed research of the effect of barium substitution on the structural, thermal, optical, electrical, dielectric and magnetic properties in order to get an overview of relaxation process and conduction mechanism as well as photoluminescence and magneto-caloric properties.

2. Experimental methods

As already mentioned above, $Ho_{1-x}Ba_xCrO_3$nanoparticles with different Ba concentrations were prepared via the sol-gel route. The precursors used were hydrated nitrates. They were mixed together using magnetic stirrer to get a homogeneous solution. The chelating agents (citric acid and ethylene glycol) were added in the ratio of [(1-x) (Ho^{3+})+x(Ba^{2+})+1 (cr^{3+}) / 1.5 (citric acid) / 2.25 (ethylene glycol)]. The mixed solution was heated at 100°C and kept under sitting for 5 hours until the gel was formed. The gel obtained was put in the oven at 200°C for 6 hours to be dried. Then , the obtained powder was ground and calcinated at 400°C, 600°C and 800°C for 4h , 6h and 10h respectively. After each heat treatment temperature, the sample was again milled to get the intended nanoparticles powder. Then, the synthesized sample was pressed to get pellets of 1.5mm thickness and 3.5mm radius. The resulting powder was analyzed by X- Ray Diffraction using D5000 Siemens diffractometer (Cuk_α radiation source, λ = 1.5406 A°, 2θ range from a low angle to 70° with a step size of 0.017) at room temperature in order to get information about phase formation, phase purity, lattice parameters and crystallite size. The Rietveld refinements were performed using Fullprof program [28]. FT-IR spectra were recorded with a Perkin-Elmer spectrophotometer

in a range of 400 to 1000 cm^{-1}. The Raman spectrum of the samples was obtained using HORIBA LABRAM HR spectrometer with an excitation wavelength of 932.8 nm. Further, Mettler-Toledo instrument was used under air atmosphere with a heating rate 10 °C/min to collect TGA and DTA data. UV-VIS-NIR diffuse reflectance spectra were recorded at room temperature using a Shimadzu UV-2501PC spectrophotometer over the spectral range 150-850 nm. The electrical and dielectric measurements were carried out using Agilent 4249 A impedance analyser over a wide range of frequencies (40Hz – 1MHz) at several temperatures (100 °C- 600°C).The experiment gave a real part Z' and an imaginary part Z" of the impedance complex Z*.The magnetic properties of the samples were measured using a vibrating sample magnetometer (VSM). The magnetization was measured from 5 to 300 K under two protocols: (i) cooling the sample in zero field (ZFC) and (ii) cooling the sample with the magnetic field applied (FC). In the following, the samples will be noted by HBCO0, HBCO2 and HBCO3 for x= 0.0; 0.2 and 0.3 respectively.

3. Results and discussion

3.1 X-ray analysis

The X-Ray Diffraction pattern of the as-prepared samples measured at room temperature is shown in **Fig.1..** The XRD pattern indicates the presence of a single phase. Rietveld refinements of the XRD data reveal that these compounds crystallise in orthorhombic distorted structure with a Pnma space group. **Fig.2** shows the schematic representations of the perovskite structure, generated using VESTA program [29]. The structural cell parameters and refinement factors are listed in Table1.

In order to examine the distortion degree after the increase of Ba amount, the Goldschmidt tolerance factor t was introduced: [13]

$$t=\frac{r_A+r_O}{\sqrt{2\left(r_B+r_O\right)}} \qquad (1)$$

Where r_A, r_B and r_O are the ionic radii of the A and B cations sites and oxygen site respectively. For the oxygen, there are two sites O1 and O2.

This factor is equal to a unity for a compound presenting an ideal cubic structure. For distorted perovskite structures, the value of t becomes less or greater than 1[13, 32, 33]. In fact, if the A ion is smaller than the ideal value, we observe the tilting of BO_6 ochtaedra in order to fill the space.

In the presentwork, based on the ionic radius of Ba $\left(r_{Ba^{2+}} = 0.134nm\right)$[34]), Ho ($r_{Ho^{3+}} = 0.0901nm$[35]), Cr ($r_{Cr^{3+}} = 0.063nm$[36]) and O ($r_{O^{2-}} = 0.14nm$[37]), and the following relation $r_A = (1-x)r_{Ho^{3+}} + xr_{Ba^{2+}}$, the tolerance factor was calculated. The obtained t values are presented in Table1. From this table, one can see that Goldschmidt factor values, for all the products, verify the relation 0.707⟨ t⟨0.9[32], which proves again the orthorhombic structure of the materials. Moreover, the prepared samples are characterised by a structure in which c/a< $\sqrt{2}$ <b attesting that the lattice distortion can be also explained in terms of cooperative Jahn-Teller effect [38, 39]. The slight increase of the ratio c/a and the increase of the Goldschmidt factor with the augmentation of Ba amount, as shown in Table, disfavour the cooperative octahedral tilting of the corner sharing CrO_6 and consequent rising of symmetry by a progressive increase of the Cr-O2-Cr bond angle(**Fig.2**)[40-42]. Additionally, the unit cell volume V increases with increasing Barium content in A site (Table 1). This growth is attributed to the ionic radius of Ba^{2+} which is larger than that of Ho^{3+}.

As shown in the inset of **Fig.1**, the full width at half maximum (FWHM) of the most intensive peak for each composite was used to obtain the average crystallite size using Scherrer's equation [43]:

$$D=\frac{0.9\times\lambda}{\beta\times\cos\theta} \qquad (2)$$

where λ is the wavelength of light used for the diffraction, β is the "full width at half maximum" of the sharp peaks and θ is the angle measured.

In addition, we have calculated the average particle size D uncertainties expressed by [44]

$$\Delta D=D\times\left(\frac{\Delta\beta}{\beta}+\frac{\Delta(\cos\theta)}{\cos\theta}\right) \qquad (3)$$

where $\Delta\beta=\pm0.01°$ and $\Delta(\cos\theta)=\pm0.001$.

The obtained results are summarized in Table1.Notably, D increases with increasing Ba concentration, which can be explained by the rise of the radius of A sites.

3.2 FT-IR analysis

The experimental IR spectra of HBCO0, HBCO2 and HBCO3 samples recorded at room temperature are shown in **Fig. 3**. The bands at 460, 549, and 610 cm^{-1} are attributed to Cr^{3+}–O bonds in the bending mode [45,46] while the vibrational modes observed at 580, 630, 715, 817 and 930 cm^{-1} are assigned to Cr^{4+}–O in the bending mode [47]. The spectra show also a broad band at around 502 cm^{-1} which is attributed to Ho^{3+}−O in the bending mode [48, 49].

3.3 Raman Analysis

In addition to the X-Ray Diffraction, Raman spectroscopy is used to perform the structural analysis of the materials. This technique is useful to detect the structural distortions caused by the octahedral rotations and/or displacement of A-cation. The Raman spectrum of the nanopowder $Ho_{1-x}Ba_xCrO_3$obtained at room temperature in the frequency range of 100 cm^{-1}-600 cm^{-1} is plotted in **Fig.4**. Theoretical studies show that the orthorhombic Pnma perovskite structure has 24 Raman-active modes: $7A_g+5B_{1g}+7B_{2g}+5B_{3g}$ [22]. From **Fig.4,** it is observed that the Raman active modes are indicative of the phase purity of our materials. The most important modes are observed at around 140, 161, 220, 260, 313, 351, 416, 484 and

570 cm^{-1}. $A_g(7)$ is attributed to the vibrational motion of O1 and A along the x-axis, $B_{2g}(5)$ describes the vibration of A-cation along the x-axis, Ag(6) is associated with the in-phase rotational vibration of the CrO_6 octahedra around the y-axis, $B_{2g}(6)$ corresponds to the vibration of A-cation and O1 along the z axis, $B_{1g}(3)$ is ascribed to the out of phase octahedral rotation around the x-axis, the $A_g(4)$ phonon mode involves mixed vibrations of A-cation and O1 along the z-axis (A(z),O1(-z)), $A_{3g}(4)$ is associated with the out-of-phase O2 scissor-like vibration and finally, B3g(2) is related to the anti-stretching vibration mode of O1 and O2 atoms [2,22,50].

It is noted that the Raman modes between 250 cm^{-1} and 450 cm^{-1} become more intense and wider as the amount of Ba increases which is associated to the structural variation by changing the values of the angles between adjacent $Cr^{3+}O_6$- $Cr^{4+}O_6$octahedral clusters [51].

On the other hand, one can see that at this frequency range, the Raman active peaks shift slightly, which is associated to the radius of A sites and the large difference between the atomic masses of Ho (164.93 u) and Ba (137.32 u)[2].

3.4 Thermal analysis

Thermal decomposition of our products has been studied by measuring the TGA-DTA, which is shown in **Fig.5.** As shown in this figure, at a 25-1000 °C temperature range, it is seen that for all samples the endothermic peak appears at ~ 80 °C with a weight loss of 0.04%. This endothermic peak appeared due to the vaporisation of surface absorbed volatile water and solvent liquid in the as-prepared samples. The exothermic rise observed in the ATD curves may be due to a slight dilatation of the materials. Globally, the TGA curves show that for all the different samples the mass losses are too low in the range of the studied temperature. The result indicates that the synthesized powders were stable.

3.5 Optical analysis

In order to obtain optical band gap, the UV-VIS-NIR absorption spectra of the $Ho_{1-x}Ba_xCrO_3$ nanoparticles were performed in UV-VIS-NIR regions using reflectance data according to the Kubelka-Munk relation [52] :

$$\alpha(\lambda) \equiv \frac{(1-R_\infty)^2}{2R_\infty} \quad (4)$$

where R_∞ is the diffused reflectance of the powder.

As shown in **Fig .6**, it is clear that all the samples exhibit strong absorption band in both UV and visible region and poor absorption in NIR region which is related to charge transfer transition.

The direct band gap energy E_g was calculated using Tauc's equation given by[52] :

$$(\alpha h\nu)^2 = B(h\nu - E_g) \quad (5)$$

where α is the optical absorption coefficient, hυ the photon energy, E_g the band gap and B the constant.

The $Ho_{1-x}Ba_xCrO_3$ samples showed two band gap energies, one of them was O(2p)-Cr(3d) charge transfer (CT) and the other was attributed to Cr 3d-d interaction 5(Mott gap) [53]. The E_g values listed in Table 2 were determined from the extrapolation of the two straight portions of the Tauc curves to zero as shown in **Fig.7**. From Table 2, one can see that the measured E_g values confirm the semiconductor behaviour of the compounds [54] and diminish with the increase of Ba content. The decrease in the band gap can be attributed to the increasing Cr-O2-Cr bond angle leading to the increase of the overlap between Cr(3d) and O(2p) levels [55].

The absorption edge follows the Urbach's formula [56] :

$$\alpha = \alpha_0 e^{\frac{h\nu}{E_u}} \quad (6)$$

where A_0 is a constant and E_u is the Urbach energy which characterize the degree of disorder in the materials.

The obtained values of E_u are estimated from the inverse of the straight portion's slopes of Ln(α) vs. the incident photon energy (hν) as shown in **Fig.8** and tabulated in Table 2. It is found that Urbach energy decrease with Ba substitution indicating a decrease of disorder in the samples [56]. This result is probably related to the fact that the structure is less distorted as Ba amount increases which is a consequence of the reduction of the effect Jahn Teller cooperative [42].

In order to identify the electronic transition implicated in the absorption process, the room temperature emission spectra of all the samples obtained under the excitation wavelength λ_{ext}=280nm were recorded in the UV, visible and near infrared ranges as shown in **Fig.9.** Four visible emission bands centred at 467 nm (blue emission), 567 nm (orange emission), 619 nm(yellow emission) and 764 nm(red emission) due to the transitions $^5F_2+^3K_8 \rightarrow {}^5I_8$, $^5F_4+^5S_2 \rightarrow {}^5I_8$, $^5F_5 \rightarrow {}^5I_8$ and $^5I_4 \rightarrow {}^5I_8$ respectively, can be observed. Two infrared emission bands appear at 824nm and 885 nm corresponding to $^5S_5 \rightarrow {}^5I_7$ and $^5I_5 \rightarrow {}^5I_8$ respectively, which can be explained by the appearance of oxygen vacancies. In these transitions, the infrared emission bands are the most intensive [57-59]. These results show a promise of new compounds used in light-emitting devices and optical communications.

3.6 Impedance spectroscopy

3.6.1 Electrical analysis

Fig.10 shows Nyquist Z'-Z'' plot of HBCO0, HBCO2 (**Fig.10a**) at one representative temperature (T=873K) and at different temperatures for HBCO3(**Fig.10b**). The complex impedance spectra display several semi-circular arcs. The measured impedance data are fitted using origin 6.0 software. An excellent agreement between the calculated and experimental curves was observed.

The diagrams consist of depressed semi-circular arcs whose center is located below the real axis, which suggests that the dielectric relaxation is of the a non-Debye type [60] in these

materials. Generally, the appearance of full or partial semicircles relies on the strength of relaxation and the experimentally available frequency domain. Furthermore, Non-Debye type of responses can be explained by the formation of the nanopolar clusters [61]. In order to analyze the experimental results, it is extremely important to have an equivalent circuit model that provides more information about electrical properties. The figure insets (**Fig.10**) present the equivalent circuits. According to Debye's model, an equivalent circuit is assembled from resistors and capacitors in parallel but for Non-Debye type of relaxation , it is customary to introduce the concept of constant phase element (CPE) replacing the ideal capacitor. It has an impedance which is given by [62]:

$$Z_{CPE}=1/A(j\omega)^{n} \quad (7)$$

In the above relation, ω is the angular frequency, A (in $F.cm^{-2}.S^{n-1}$[62]) and n ($0<n<1$) are frequency independent constants. The latter characterizes the deviation from the ideal behaviour. The case n=1 represents a pure capacitance, whereas n=0 represents a pure resistance.

In **Fig.10a**, the equivalent circuit is symbolized by a parallel composition of a resistor and constant phase element (CPE). In this case, the total impedance $Z^{*}(\omega)$ of these samples can be described by the following equation:

$$Z^{*}(\omega) = Z'+jZ'' = (1/Rg+1/ Z_{CPE})^{-1} \quad (8)$$

Where Z' and Z'' are attributed to real and imaginary parts of the complex impedance. The fitting of these semicircles is based on the following relationships:

$$Z' = \frac{R_g(1+R_gA_g\,\omega^{n_g}\cos(\frac{n_g\pi}{2})}{1+2R_gA_g\,\omega^{n_g}\cos(\frac{n_g\pi}{2})+(R_gA_g\omega^{n_g})^2} \quad (9)$$

$$-Z'' = \frac{(R_g)^2A_g\,\omega^{n_g}\sin(\frac{n_g\pi}{2})}{1+2R_gA\,\omega^{n_g}\cos(\frac{n_g\pi}{2})+(R_gA_g\,\omega^{n_g})^2} \quad (10)$$

However in **Fig.10b**, as shown in the inset, the electrical response of the sample is modeled by an equivalent circuit containing two successively connected Resistor-CPE units put in parallel corresponding to grain and grain boundary, respectively. In the present case, $Z^*(\omega)$ is given by:

$$Z^*(\omega) = Z'+jZ'' = (1/R_g + 1/Z_{CPEg})^{-1} + (1/R_{gb} + 1/Z_{CPEgb})^{-1} \quad (11)$$

The real and imaginary part expressions for fitting are:

$$Z' = \left(\frac{R_g(1+R_g A_g \omega^{n_g} \cos(\frac{n_g \pi}{2})}{1+2R_g A_g \omega^{n_g} \cos(\frac{n_g \pi}{2}) + (R_g A_g \omega^{n_g})^2} + \frac{R_{gb}(1+R_{gb} A_{gb} \omega^{n_{gb}} \cos(\frac{n_{gb} \pi}{2})}{1+2R_{gb} A_{gb} \omega^{n_{gb}} \cos(\frac{n_{gb} \pi}{2}) + (R_{gb} A_{gb} \omega^{n_{gb}})^2} \right) \quad (12)$$

$$-Z'' = \left(\frac{(R_g)^2 A_g \omega^{n_g} \sin(\frac{n_g \pi}{2})}{1+2R_g A_g \omega^{n_g} \cos(\frac{n_g \pi}{2}) + (R_g A_g \omega^{n_g})^2} + \frac{(R_{gb})^2 A_{gb} \omega^{n_{gb}} \sin(\frac{n_{gb} \pi}{2})}{1+2R_{gb} A_{gb} \omega^{n_{gb}} \cos(\frac{n_{gb} \pi}{2}) + (R_{gb} A_{gb} \omega^{n_{gb}})^2} \right) \quad (13)$$

R_g and A_g, respectively refer to the resistance and the capacitance of grain, while R_{gb} and A_{gb} refer to the resistance and the capacitance of grain boundaries, which proves the existence of space charge polarisation. n_g and n_{gb} are associated to the exponential index of grain and grain boundaries. These fitting parameters are given in Table 3. As illustrated in Table 3, the values of the exponential index are relatively close to 1, which signifies that the deviation from Debye behaviour isn't very strong. It is observed that the grains resistance decreases with the increase of the Ba substitution (Table 3) but also with increasing the temperature (**Fig.10b)**. The decrease of grain resistance results in the increase of conductivity.

In order to understand the effect of substitution on the conduction process, the DC conductivity was measured as a function of the temperature as shown in **Fig.10** using the following relation:

$$\sigma_{DC} = e/SZ_0 \quad (14)$$

where e is the sample thickness, S is the sample area and Z_0 corresponds to the interception of the real axis with the lowest frequency curve.

It is clear that the increase in temperature increases the value of conductivity, denoting the semiconducting behaviour and a thermally activated conduction in our compounds. We have analysed our experimental data with the Arrhenius model for HBCO0 and HBCO2, whereas for HBCO3, the results obtained are interpreted according to Mott's VRH model. The activation energies are calculated from the Arrhenius plots (**Fig.11)** in accordance with the relationship [61, 63]:

$$\sigma_{DC} = \sigma_0 \exp(-E_a/K_BT) \quad (15)$$

where σ_0 the pre-exponential factor, E_a the activation energy, K_B Boltzmann constant and T the absolute temperature. The E_a values were found to decrease with increasing the amount of Ba in the samples (Table 4). These values suggest that the conduction mechanism can be explained by the polaron hopping between the nearest neighbouring sites [61, 63, 64]. In this case of mixed-valence chromites, the formation of the polaron Cr^{4+}-O-Cr^{3+} can be related to charge carriers localization [64] which is a direct consequence of cooperative Jahn Teller distortion [65]. As already mentioned, such an effect was found to decrease with the increase of the Ba content, leading to the increase of the electronic bandwidth W given by [6, 66, 32]:

$$W \approx \frac{\cos\left(\frac{\pi-\gamma}{2}\right)}{\left(d_{Cr-O}\right)^{3.5}} \quad (16)$$

where γ is the Cr-O2-Cr bond angle and d_{Cr-O} is the Cr-O bond lengh.

W is characterised by the spatial overlap between the Cr(3d) an O(2p) orbitals . Further, the rise of the width conduction band W (decrease of E_a), controlled by the decrease of d_{Cr-O}, can be confirmed not only by the increase of the tolerance factor value (Table 1)[32,13] but also by the decrease of the direct band gap E_g as already mentionned.

In addition, the decrease of the activation energy can be justified by the increase of the cell volume of the samples (Table1) according to Wakamura's relationship [67]:

$$E_a = A_v/V^{2/3} \quad (17)$$

where A_v is a constant, and V is lattice volume.

However, for HBCO3, the conduction mechanism was described by VRH model. In fact, at low temperatures, the thermal energy is not sufficient to allow the electron hopping between the nearest neighbour sites but is possible to hop further to find a localized state with a smaller potential difference. The conductivity data were fitted using Mott's law [68]:

$$\sigma_{DC} = \sigma_0 \exp\left(-(T_0/T)^{1/4}\right) \quad (18)$$

where σ_0 and T_0 are constant.

According to the VRH mechanism, the Mott characteristic temperature T_0 is given by [68, 69]:

$$T_0 = 24/\pi K_B N(E_F)\xi \quad (19)$$

where $N(E_F)$ is the electronic density of states at the Fermi level and ξ is the radius of localization length .

The hopping distance R_{hop} and hopping energy W_{hop} can be written at a given temperature as[68,69]:

$$R_{hop} = \xi^{1/4} / [8\pi N(E_F) K_B T]^{1/4} \quad (20)$$

$$W_{hop} = 3/[4\pi R_{hop}^3 N(E_F)] \quad (21)$$

From the linear fitting to the experimental data, we found, by taking ξ= 1.729A° [70], that T_0 =1.107 10^7 K and $N(E_F)$=1.547 10^{21} $(eV)^{-1}Cm^{-3}$ .The calculated values of R_{hop} and W_{hop} are tabulated in Table 5. From this table, it can be seen that, as temperature increases, the hopping distance decreases and the energy hopping increases. The hopping distance R_{hop} and the bandwidth are correlated. In fact, the diminution of R_{hop} enlarges the bandwidth which in turn increases the electrical conductivity [13].

To identify the nature of conduction mechanism, the AC electrical conductivity was measured in accordance with the relationship [71]:

$$\sigma_{AC} = e\, Z'/S(Z'^2+Z''^2) \quad (22)$$

Fig.12a shows the frequency dependence of AC conductivity σ_{AC} at 873 K for Ba concentration x=0.0 and at several temperatures for HBCO3 (**Fig.12b**).

By analyzing these plots, it is observed that a low-frequency independent region corresponding to the DC conductivity is followed by a high frequency dependent region where conductivity increases with the increase in frequency. The frequency at which the transition between the two regions occurs is called the frequency hopping noted f_{hop}. From f_{hop} we can calculate the hopping time τ_{hop} ($f_{hop}=1/\tau_{hop}$). The origin of the frequency dependence of AC conductivity lies in the hopping of mobile charge carriers. At high frequencies, it is noticed that curves come closer to each other, revealing the presence of space charges [72]. Further, the curves exhibit an increase of the conductivity by raising the amount of Ba(**Fig.12a**) or the temperature(**Fig.12b**).

The phenomenon of conductivity dispersion can be explained using Jonscher'power law [60]:

$$\sigma_{AC=}\sigma_{DC}+A_1 f^{S1}+A_2 f^{S2} \quad (23)$$

where σ_{DC} is DC conductivity, A_1 and A_2 are constant factors, f frequency, S_1 and S_2 the power law exponents varying between 0 and 1. S_1 and S_2 depend on frequency and temperature.

In addition, the behavior of the power law exponent as a function of temperature is a powerful tool to identify the nature of conduction. That is why various theoretical models have been proposed to explain the conduction mechanism based on the S(T) relation. The temperature dependence of S_1 and S_2 for the samples under investigation as obtained from fitting the experimental data is shown in **Fig.13**. First, we can notice that the two parameters vary in the same way. For HBCO0, it is clear that S_1 and S_2 increase when increasing the temperature, suggesting that the non-overlapping small polaron tunneling (NSPT) modelis suitable for the present compounds. In this model, small polarons are formed when a charge carrier deforms

the surrounding lattice and a tunneling process is responsible for conductivity.According to this model, the exponent is given by[71,73]:

$$S_{1,2}=1-4/(\ln(1/\omega\tau_0)-W_H/K_BT) \quad (24)$$

where W_H is the polaron hopping energy, τ_0 is a characteristic relaxation time , K_B is the Boltzmann Constant and ω is the angular frequency. For HBCO2, the values of S_1 and S_2 decrease with the increase in temperature. Such a behavior can be described by the correlated barrier model (CBH). In this model, the conduction happens via charge carriers hopping process over the Coulomb barrier separating the localized sites. In CBH model, the exponent is evaluated as follows [73]:

$$S_{1,2}=1-6K_BT/W_M-K_BTLn(1/\omega\tau_{0)} \quad (25)$$

Here, W_M is the binding energy and τ_0 the atomic vibration period

For HBCO3, the exponents are found to have two different trends. In the temperature range 373 K to 473 K, it is noted that the exponent, firstly, decreases with increasing temperature till 423 K and thereafter shows an increasing trend up to 473K. Here, the most suitable model for the present sample, to interpret the conduction mechanism, is the overlapping large polaron tunneling (OLPT). According to OLPT model, the large polaron wells of two sites overlap lowering the polaron hopping energy and the power law exponent follows [74]:

$$S_{1,2} = 1-\ (8\alpha R_\omega+6W_{HO}\ r_0/R_\omega K_BT)/(2\alpha R_\omega+W_{HO}\ r_0/R_\omega K_BT)^2 \quad (26)$$

where r_0 is the large polaron radius, W_{HO} is a constant for all sites, R_ω hopping length at the angular frequency ω (tunneling distance) and α is inverse localization length. Whereas, for the range from 473 K to 573 K, it is clear that as the temperature increases, the S_1 and S_2 decrease, suggesting that the conduction mechanism can be elucidated by CBH model.

3.6.2 Dielectric analysis

The complex permittivity $\boldsymbol{\varepsilon}^*$ is expressed by [43]:

$$\boldsymbol{\varepsilon}^*=\boldsymbol{\varepsilon}'(\omega)-j\boldsymbol{\varepsilon}''(\omega) \quad (27)$$

where the real part ε' named dielectric constant and the imaginary part are given by :

$$\varepsilon' = -Z''/\omega C_0(Z'^2+Z''^2) \quad (28)$$

$$\varepsilon'' = -Z'/\omega C_0(Z'^2+Z''^2) \quad (29)$$

where $C_0=eS/\varepsilon_0$(e and S are the pellets thickness and area respectively) is the capacitance of the empty cell. From the last expressions we can define the dielectric loss as [43,75]:

$$\tan\delta = \varepsilon''/\varepsilon' \quad (30)$$

Fig.14 and **Fig.15** exhibit the dielectric constant ε' and dielectric loss tanδ vs. frequency respectively. As can be seen from these figures, for all the compounds, both ε' and tanδ decrease on increasing frequency, revealing dispersion behavior at low frequency range. Such a behavior is commonly observed in polar dielectric materials [76].

From the plots, it is visible that dielectric constant is higher at low frequencies. It is well-known that the polarization of dielectric material results from the contributions of all polarization types (interfacial, dipolar, ionic and electronic) [77]. At low frequencies, ε' is maximum because the space charge polarization and dipolar polarization are the most important [77], but as the frequency of the applied electric field increases, more and more space charges are unable to follow the rapid variations of the external applied field as well as dipoles leading to the diminishing of polarization[64,77] and hence ε' decreases. Analogously, the dielectric loss decreases in the same way as dielectric constant.

On the other hand, on decreasing temperature, ε' and tanδ rise slightly, indicating that the dielectric relaxation in the samples is thermally activated [78]. Further, it must be noted that for x=0.3, the best values of ε' were observed with the lowest dielectric loss as compared with the other prepared compounds. In fact, Table 6 summarizes the best results obtained in the case of x=0.3 and shows the comparison of our work with other compounds reported in the literature. These properties offer an excellent promise to this product for technologically important dielectric applications such as memory devices and capacitors.

3.6.3 Modulus analysis

Modulus formalism is another method to analyze the relaxation phenomenon. The complex electric modulus M* corresponds to the relaxation of the electric field in the system when the electric displacement is constant. M* was obtained from the complex dielectric permittivity using the following relation [77]:

$$M^* = 1/\varepsilon^* = M' + j\,M'' \qquad (31)$$

where M' and M'' are respectively the real and imaginary parts of modulus.

Fig.16 shows the M'' vs. frequency at different temperatures for all the prepared samples. M'' spectrum is characterized by the appearance of slightly asymmetrical peaks, suggesting non-Debye type dielectric relaxation [75] but close to ideal behavior. The peaks shift towards the higher frequency side with increase in temperature as well as Ba content hence time relaxation decreases. Such behavior is attributed to the correlation between motions of charges carriers and indicates that the dielectric relaxation process is thermally activated. The relaxation time τ associated to each peak is calculated from the frequency at which the maxima of M'' occurs. The frequency range below peak maximum is associated to the region in which charge carriers are mobile on long distances. However, at frequency above peak maximum, the carriers are cramped to potential wells, being mobile on short distances [64, 75]. Further, an exception is observed in the case of HBCO3. In fact, two peaks are observed. One appears at low frequency region and the other at high frequency region which are essentially associated to the relaxation process of grains and grain boundaries [83].

In order to explain the asymmetric nature of peaks, the experimental data was fitted using the following modified KWW function suggested by Bergman [84] :

$$M'' = \frac{M''_{Max}}{(1-\beta)+\frac{\beta}{1+\beta}\left[\beta\left(\frac{f_p}{f}\right)+\left(\frac{f}{f_p}\right)^{\beta}\right]} \qquad (32)$$

where M''_{max} is the peak maximum of the imaginary part of the modulus, f_{max} is the peak frequency ofthe imaginary part of the modulus and β (0< β<1) is the stretched exponent parameter indicating the deviation from Debye-type relaxation (β=1). This parameter is also related to the interaction between mobile charges carriers.

The values of β are given in Table 7 and are found to be less than unity for all the compounds. This confirms the non-Debye type of the dielectric relaxation process. From Table7, one can see the slight increase of β with the rise of temperature and Ba amount indicating a decrease in the correlation between the charge carrier and its vicinity.

3.7 Magnetization analysis

Fig .16 shows the hysteresis loops of $Ho_{1-x}Ba_xCrO_3$ (x = 0.0, 0.2, 0.3) samples measured at 5 K and $HoCrO_3$ at room temperature. These measurements were collected using the magnetic field (H) range [-10, 10 T] for x=0.2 and x=0.3, and [-5,5T] for x=0.0.

It is clear that all the samples exhibit a nonlinear magnetization dependence on the magnetic field at 5 K. In addition, they showed a weak ferromagnetic behaviour and the saturation phenomenon increases slightly with increasing Ba amount. The enhanced ferromagnetic magnetization in Ba-substituted $HoCrO_3$ compounds can be correlated to the lattice structural change in Cr-O-Cr bond angle and Cr-O bond distance which induces a variation of the volume as shown in Table 1 inducing the formation of oxygen vacancies and a decrease in cooperative Jahn-Teller effect as already mentioned. In fact, the increase of Cr-O2-Cr bond angle (approaching to the ideal case of 180°) leads to the increase in the double exchange interaction and thus increases 3d (Cr)-2p (O) hybridation and the bandwidth in the material. Further, the increase of A-site ionic radii enlarges the bandwidth W via the variation of the Cr-O2-Cr bond angle and Cr-O bond length. The increase of W, as the Ba amount increases, leads to a narrowing of the band gap energy, suggesting the weak ferromagnetism

enhancement. Additionally, the presence of magnetic moment at the A site improves the magnetization owning to the polarisation of the rare earth Ho^{3+} by Cr^{3+} [85-87].

The enhancement of magnetization with Ba^{2+} concentration was previously observed by M.M. El-Desoky et al [88], S.K. Mandal et al. [89] and G. Dhir [90]. On the other hand, HBCO0 remains in a linear paramagnetic phase at 300 K.

The temperature dependence of magnetization with zero-field cooling (ZFC) and field cooling (FC) obtained at a field of 0.2T are shown in **Fig .18**. In all the samples, we can observe a bifurcation around 143K which is attributed to the magnetic ordering of Cr^{3+} sub-lattice [91]. At temperatures above T_N=143K (Neel Temperature), the paramagnetic behavior is dominant, while below this temperature there is a weak ferromagnetic behavior for all the samples. The net magnetic moment is associated to the small canting angle of the Cr^{3+} spin moments followed by the tilting of two adjacent CrO_6 corner-sharing octahedra, with a Cr-O2-Cr bond angle ≤180°. Just below T_N, the magnetic properties are dominated by Cr^{3+}magnetic moments which order antiferromagnetically through the superexchange mechanism and the Ho^{3+}- Ho^{3+} sublattice orders at very low temperatures (2 - 15 K) [92]. Moreover, ZFC measurements of $HoCrO_3$ did not show negative magnetization. However, at very low temperatures, HBCO2 and HBCO3 show negative magnetization which is assigned to diamagnetic phase due to the anti-parallel ordering of the paramagnetic Ho^{3+} and the Cr^{3+} magnetic moments [93,94].

To obtain the magnetocaloric effect, the isothermal magnetization M (μ_0H) curves measured at various temperatures around the Neel temperature for $Ho_{1-x}Ba_xCrO_3$ compounds are shown in **Fig.19**. As we can see, the isotherm plots exibit a linear rapid increase for all the samples. Such a behaviour seems to be similar to that of the compound $La_{0.4}Ca_{0.6}MnO_3$ [95]. Further, the magnetization of the investigated samples does not saturate suggesting the presence of spin disorder in the system, with Cr^{3+} and Cr^{4+} ions in different spin states together with the ferrimagnetic Ho^{3+} and paramagnetic Ba^{2+} ions.

The magnetocaloric effect is determined in terms of isothermal magnetic entropy change ΔS using the magnetization isotherms around the transition temperature T_N and by utilizing Maxwell's relationship:

$$\left(\frac{\partial S(H,T)}{\partial H}\right)_T = \left(\frac{\partial M(H,T)}{\partial T}\right)_H \quad (33)$$

$$\Delta S(T,\Delta H) = \int_0^{\mu_0 H}\left(\frac{\partial S(T,H)}{\partial H}\right)_T dH = \int_0^{\mu_0 H}\left(\frac{\partial M(T,H)}{\partial T}\right)_H dH \quad (34)$$

Hence, ΔS can be numerically calculated using Eq (35) and the measured magnetization as a function of magnetic applied field and temperature [96].

$$\Delta S(T,H) = \sum_i \frac{M_{i+1}(T_{i+1},H) - M_i(T_i,H)}{T_{i+1} - T_i}\Delta H_i \quad (35)$$

Where M_i and M_{i+1} are the magnetization values measured under a magnetic field ΔH_i, at T_i and T_{i+1}, respectively.

Fig.20 shows the temperature dependence of the magnetic entropy change under the magnetic applied field changes of 5T for HBCO0, HBCO2 and HBCO3 samples.

The (-ΔS) exhibits a maximum near the Neel temperature ($T_N \approx 143$ K). It is noticed that it increases from 3.22 J /kg K for x = 0.0 to 5.79 J/Kg K for x = 0.3 under magnetic field 5T.

The large magneto-caloric effect observed in these materials can be associated to its sharp magnetization change at the antiferromagnetic-paramagnetic transition as well as the presence of nano-crystallite field effects. Another important parameter of refrigerant materials is the relative cooling power (RCP) which is used to evaluate the cooling efficiency of a magnetic material for applications in magnetic refrigeration. The (RCP) is given by the following equation [96]:

$$RCP = -\Delta S_M^{max} \times \delta T_{FWHM} \quad (36)$$

where, δT_{FWHM} is the full-width at half maximum peak and $-\Delta S_M^{max}$ is the maximum value of magnetic entropy change.

In order to examine the usefulness of our samples, we made a comparative study of T_N, $-\Delta S_M^{max}$ and RCP with other magneto-caloric materials found in literature with low temperature magnetic transitions. The results are summarized in Table 7.

Conclusion

The $Ho_{1-x}Ba_xCrO_3$(x=0.0, 0.2, 0.3) nanoparticles were prepared by sol-gel route. The Rietveld refinement of XDR data showed that all samples show a distorted orthorhombic structure with a Pnma space group which is confirmed by Raman spectroscopy. Raman analysis gives evidence for the formation of polarons whose origin is the Jahn-Teller distortion. This effect was found to decrease with the increase of Ba content. From thermal analysis, we can conclude that the products are thermally stable. The room temperature UV/VIS/NIR diffuse reflectance spectra indicate that the as-prepared samples are in a direct band gap materials with a strong UV-Visible absorption band indicating that these materials are good candidates for solar cells. Pl spectra exhibit a significant emission in both visible and Near-infrared regions. Such a result may be fruitful for future optoelectronic applications of these materials.

The impedance spectroscopy showed that the dielectric relaxation is of non-Debye type.

The variation of DC conductivity as a function of temperature exhibits that while the compounds HBCO0, HBCO2 obey the Arrhenius law with activation energies of 0.518, 0.491, 0.452 respectively, the HBCO3 is found to obey Mott's law. The values of activation energy lead us to conclude that conduction is due to polaron hopping based on the electron carriers. The AC conductivity was found to obey Jonscher's law. As a result, the conductivity mechanism in the materials was explained based on the temperature dependency of the

exponent S. The dielectric properties of the samples under investigation were studied and explained in view of interfacial polarization. Exceptionally, for x=0.3, high values of dielectric constant and low dielectric loss, especially in low frequency range, were observed. Such a finding makes this product an attractive candidate for several industrial applications. Modulus formalism showed similar behavior as impedance spectroscopy (non Debye behavior) and a short relaxation time. Here, again, HBCO3 presents the exception that it shows two peaks related to grains and grains boundaries contributions to electrical response.

From magnetic measurements, we discover a large magnetocaloric effect which makes the present samples excellent candidate for magnetic refrigerators at low temperature.

Acknowledgments

The authors thank FEDER funds through the COMPETE 2020 Program and National Funds through FCT – Portuguese Foundation for Science and Technology under the project UID/CTM/50025/2013 and UID/FIS/04564/2016.

References :

[1] L.H.Yin, J.Yang, R. R.Zhang, J. M. Dai, W. H. Song, and Y. P. Sun, Multiferroicity and magnetoelectric coupling enhanced large magnetocaloric effect in $DyFe_{0.5}Cr_{0.5}O_3$, Appl. Phys.Lett, 104 (2014),032904

[2]M. C. Weber, J. Kreisel, P. A. Thomas, M. Newton, K. Sardar, and R. I. Walton**,** Phonon Raman scattering of $RCrO_3$ perovskites (R=Y, La, Pr, Sm, Gd, Dy, Ho, Yb, Lu), Phys.Rev.B, 85(2012), 054303.

[3]S.Yin, T.Sauyet, M.S. Seehra, and M.Jain, Particle size dependence of the magnetic and magneto-caloric properties of $HoCrO_3$, J.Appl.Phys, 121(2017), 063902.

[4]K.Sardar, M.R. Lees, R.J. Kashtiban, J.Sloan, R. I. Walton, Direct Hydrothermal Synthesis and Physical Properties of Rare-Earth and Yttrium Orthochromite Perovskites, Chem.Mater, 23(2011), 48-56.

[5]A.C.Komarek, S.V.Streltsov, M.Isobe, T.Möller, M.Hoelzel, A.Senyshyn, D.Trots, M.T. Fernandez-Dıaz, T.Hansen, H.Gotou, T.Yagi, Y.Ueda, V.I.Anisimov, M.Gruninger, D.I. Khomskii and M.Braden, CaCrO3: An Anomalous Antiferromagnetic Metallic Oxide, Phy.Rev.Lett, 101(2008), 167204.

[6]V.Hreb, L.Vasylechko,V. Mykhalichko, Y. Prots, Anomalous Thermal Expansion of $HoCo_{0.5}Cr_{0.5}O_3$ Probed by X-ray Synchrotron Powder Diffraction, Nanoscale.Res.Lett, 12 (2017), 442.

[7]S.Yin,T.Sauyet, C.Guild, S.L.Suib, M.Jain, Magnetic properties of pure and Fe doped $HoCrO_3$ thin films fabricated via a solution route, J.Magn.Magn. Mater, 428(2017), 313-319.

[8]A.Lund, T.Jacobsen, K.Vels, Hansen, M.Mogensen, Composite Sr- and V-doped $LaCrO_3$/YSZ sensor electrode operating at low oxygen levels, J.Solid State Electrochem, 16(2012), 2113–2120.

[9]J.Shanker, M.B.Suresh,G.N.Rao, D.S.Babu, Colossal dielectric, relaxor ferroelectric, diamagnetic and weak ferromagnetic properties of $NdCrO_3$ perovskite nanoparticles, J.Mater. Sci, 54(2019), 5595–5604.

[10]A.P.B.Selvadurai, V.Pazhanivelu, C.Jagadeeshwaran, R.Murugaraj, I.P.Muthuselvam, F.C.Chou, P.M.Md Gazzali, G. Chandrasekaran, Structural, magnetic and electrical analysis of $La_{1-x}Nd_xCrO_3$ ($0.00 < x < 0.15$): synthesised by sol–gel citrate combustion method, J.Sol-Gel.Sci.Technol, 80(2016), 827–839.

[11]M.Sun, Y.Jiang, F.Li, M. Xia, B. Xue and D.Liu, Dye Degradation Activity and Stability of Perovskite-Type $LaCoO_{3-x}$($x=0\backsim0.075$), Trans.Mater, 51(2010), 2208-2214.

[12]M.W.Lufaso, P.M.Woodward, Jahn -Teller distortions, cation ordering and octahedral tilting in perovskites, Acta.Crystallogr B, 60(2004), 10-20.

[13]Ch-Y.Chou, N. Kaurav, Y-K. Kuo and D-H.Kuo, Electrical properties of A/B –site substituted Ni-deficient $La(Ni_{0.6}Fe_{0.3})O_3$ perovskites with $A=Ag^{+}$, Pb^{2+}, Nd^{+3} and $B=Mn^{3+}$, Ga^{3+}, J.Appl.Phys, 103(2008),093716.

[14]V.Drozd, M.Pekala, J.Kovac, I.Skorvanek, M.Szymanski and S. Nedilko, Structure and Transport Properties of $La_{0.75-x}RE_xCa_{0.25}MnO_3$ (RE=GD, Dy, Ho; $0\leq x\leq0.75$) Manganites, Acta.Phys.Pol, 106(2004), 751-758.

[15]J.Qi, Z.Gui, W.Li, Y.Wang, Y.Wu, L.Li, Temperture stable $Ba_{1-x}Cd_xTiO_3$ dielectrics, Mater.Lett, 56(2002), 507.

[16] H.P.S.Corrêa, C.O.Paiva-Santos, L.F.Setz, L.G.Martinez, Crystal structure refinement of Co-doped lanthanum chromites, Powder Diffr, 23(2008), 18-22.

[17] X.Rui1, J.Walter, Ch.Leighton, R.Klie, Atomic-resolution study of oxygen vacancy ordering in $La_{0.5}Sr_{0.5}CoO_{3-\delta}$ thin films on $SrTiO_3$ during in situ cooling experiments, Microsc. Microanal.Res, 24(2018), 84-85.

[18] D.A.Kumar, S. Selvasekarapandian, H. Nithya, J.Leiro, Y.Masuda, S.D.Kim, S.K. Woo, Effect of calcium doping on $LaCoO_3$ prepared by Pechini method, Powder Technol, 235(2013),140–147.

[19] P.V.Balachandran, J.M.Rondinelli, Interplay of octahedral rotations and breathing distortions in charge ordering perovskite oxides, Phys. Rev. B, 88(2013), 054101.

[20] Sh.Yin, V.Sharma, A.McDannald, F.A.Reboredo and M.Jain, Magnetic and magneto-caloric properties of iron substituted holmium chromite and chromite, RSC adv, 6(2016), 9475-9483

[21]W.Zhang, J.Tang, J.Ye, Structural, photocatalytic, and photophysical properties of perovskite $MSnO_3$(M = Ca, Sr, and Ba) photocatalysts, J.Mater.Res, 22(2007), 1859-1871.

[22]V.R.Mannepalli, M.M.Saj Mohan, R.Ranjith,Tailoring the bandgap and magnetic properties by bismuth substitution in neodymium chromite, Bull.Mater.Sci, 40(2017), 1503-1511.

[23]A.J.Zhou, T.J.Zhu, X.B.Zhao, Thermoelectric properties of perovskite-type oxide $La_{1-x}Sr_xCoO_3$ (x = 0, 0.1) prepared by solid state reactions, Mater.Eng.B, 128(2006), 174-178.

[24]S.Nakayama, M.Okazaki, Y.L.Aung,M.Sakamoto, Preparations of perovskite-type oxides $LaCoO_3$ from three different methods and their evaluation by homogeneity, sinterability and conductivity, Solid State Ion,158(2003), 133-139.

[25]Ch.Chen, J.Cheng, Sh.Yu, L.Che, Z.Meng, Hydrothermal synthesis of perovskite bismuth ferrite crystallites, J.Crist.Growth, 291(2006), 135-139.

[26]K.Ridaa, M.A.Peña, E.Sastre,A.Martinez-Arias, Effect of calcination temperature on structural properties and catalytic activity in oxidation reactions of $LaNiO_3$ perovskite prepared by Pechini method, J.Rare.Earth, 30(2012), 210-216.

[27]H.E.Figen, N.O. Guidal and S.Z. Baykara, Preparation and Characterization of $LaMoO_3$, $La_xSr_yV_zO_3$ and $La_xSr_yMo_zO_3$ Perovskite Type Oxides by the Sol-Gel Citrate Method , Acta Phys.Pol, 125(2014),278-280.

[28]J. Rodriguez-Carjaval, Recent advances in magnetic structure determination by neutron powder diffraction, Physica B Condens Matter , 192(1993), 55.

[29] K. Momma, F.Izumi, VESTA 3 for three-dimensional visualization of crystal, volumetric and morphology data, J. Appl. Crystallogr, 44 (2011), 1272-1276.

[30] N.F. Atta, A. Galal, S.M. Ali, The Effect of the Lanthanide Ion-Type in $LnFeO_3$ on the Catalytic Activity for the Hydrogen Evolution in Acidic Medium, Int.J.Electrochem.Sci, 9 (2014), 2132 – 2148.

[31]R. Kannan, D. Vanidha, A. Arunkumar, High temperature electrical transport properties of nanophasic $Ba_{1-x}Sb_xMnO_3$, Int J Eng Sci, 5(2013), 1211-1219.

[32]R.S.Liu, C.H.Shen, S.F.Hu, J.M.Chen, Chemical pressure control of Curie temperature in $La0.6(Ba_{0.4-x}Ca_x)MnO_3$, Mater.Chem.Phys, 75(2002), 26-31.

[33]R.Mouta, R.X.Silva and C.W.A, Paschoal, Tolerance factor for pyrochlores and related structures, Acta.Cryst B, 69(2013), 439-445.

[34]Ö. Tunusoglu, T. Shahwan, A. E. Eroglu, Retention of aqueous Ba^{2+} ions by calcite and aragonite over a wide range of concentrations, Characterization of the uptake capacity, and kinetics of sorption and precipitate formation, Geochem.J, 41(2007), 379-389.

[35]K.J.Khan, F.Saleemi, T.Abbas, I.Sadiq, Substitutional effect of rare earth element ho^{3+} on structural and magnetic properties of yttrium iron garnets, J.Ovonic.Res, 11(2015), 263-270.

[36]D.Gingasu, L.Diamandescu, I.Mindru, G.Marinescu, D.C.Culita, J.M.Calderon-Moreno, S.Preda, C.Bartha, L.Patron, Chromium Substituted Cobalt Ferrites by Glycine-Nitrates Process, Croat. Chem. Acta, 88(2015), 445-451.

[37]R.D.Shannon and C.T.Prewitt, Effective ionic radii in oxides and fluorides, Acta.Cryst, 25(1969), 925.

[38] N. Sdiri, M. Bejar, E. Dhahri, The effect of the B-site size on the structural, magnetic and electrical properties of $La_{0.7}Ca_{0.3}MnO_{3-\delta}$ compounds, J.Magn.Magn.Mater, 311(2007), 512-516.

[39] A. Moure, T. Hungría, A. Castro, J.G.O. Peña, J. Tartaj, C. Moure, Mechanosynthesis of the Orthorhombic Perovskites $ErMn_{1-x}Ni_xO_3$ (x=0, 0.1) : Processing and Characterization of Nanostructured Ceramics, Chem.Mater, 22(2010), 2908-2915

[40]B.J.Kennedy, I.Qasim and K.S.Knight, Low temperature structural studies of $SrSnO_3$, J. Phys.Condens.Matter, 27(2015), 365401.

[41]Y.Inaguma, T.Tsuchiya, T.Katsumata, Systematic study of photoluminescence upon band gap excitation in perovskite-type titanates $R_{1/2}Na_{1/2}TiO_3$: Pr (R= La, Gd, Lu, and Y), J.Solid State Chem, 180 (2007), 1678-1685

[42]H.Wahab, Effect of A – Site disorder on the bonding mechanism and optical properties of $Sm_x(Al_2O_3)_{1-x}$ system, Physica B Condens Matter, 481(2016), 24-31.

[43]S.Dash, R.N.P.Choudhary,P.R.Das,A.Kumar, Structural, dielectric and multiferroic properties of $(Bi_{0.5}K_{0.5})(Fe_{0.5}Nb_{0.5})O_3$, Can.J.Phys, 93(2015), 738-744.

[44]N.Sdiri, H.Elhouichet, E.Elakermic, A.Dhifallahd, M.Ferid, Structural investigation of amorphous $Na_2O–P_2O_5–B_2O_3$ correlated with its ionic conductivity, J. Non-Cryst. Solids, 409(2015), 34-42.

[45]S.Music, M.Maljkov, S.Popovi, R.Trojko, Formation of chromia from amorphous chromium hydroxixe, Croat Chem Acta, 72 (1999), 789- 802.

[46]B.T.Sone, E.Manikandan, A.Gurib-Fakim and M.Maaza, Single-phase α-Cr_2O_3 nanoparticles' green synthesis using Callistemon viminalis' red flower extract, Green Chem Lett Rev, 9(2016), 85–90.

[47]S.Dwivedi, J.Jadhav, H.Sharma, S.Biswas, Pulsed laser deposited ferromagnetic chromium dioxide thin films for applications in spintronics, Phys.Procedia, 54(2014), 62 – 69.

[48]S.M.Derazkola, S.Z.Ajabshir, M.S.Niasari, Novel simple solvent-less preparation, characterization and degradation of the cationic dye over holmium oxide ceramic nanostructures, Ceram.Int, 41(2015), 9593-601.

[49]L.M.S.El-Deen, M.S.A. Salhi, M.M.Elkholy, IR and UV spectral studies for rare earths-doped tellurite glasses, Jallcom, 465(2008), 333-339.

[50]N.D.Todorov, M.V.Abrashev, V.G.Ivanov, G.G.Tsutsumanova, V.Marinova, Y.-Q. Wang, and M.N.Iliev, Comparative Raman study of isostructural $YCrO_3$ and $YMnO_3$: Effects of structural distortions and twinning, Pys.Rev.B, 83(2011), 224303.

[51]M.L.Moreira, E.C.Paris, G.S.do Nascimento,V.M.Longo, J.R.Sambrano, V.R.Mastelaro, M.I.B.Bernardi, J.Andrés, J.A.Varela, E.Longo, Structural and optical properties of $CaTiO_3$ perovskite-based materials obtained by microwave-assisted hydrothermal synthesis: An experimental and theoretical insight, Acta Mater, 57(2009), 5174-5185.

[52]J.H.Im, J.Chung, S.J.Kim and N.G.Park, Synthesis, structure, and photovoltaic property of a nanocrystalline 2H perovskite-type novel sensitizer ($CH_3CH_2NH_3$)PbI_3, Nanoscale Res Lett, 7(2012), 353.

[53]T.Arima, Y.Tokura and J.B.Torrance, Variation of optical gaps in perovskite-type 3d transition-metal oxides, Phys. Rev. B, 48(1993), 17006.

[54]W. Haron, A.Wisitsoraat, U.Sirimahachai and S.Wongnawa, A simple synthesis and characterization of $LaMO_3$ (M=Al, Co, Fe, Gd) perovskites via chemical co-precipitation method, Songklanakarin J. Sci. Technol, 40(2018), 484-491.

[55]R.Prasanna, A.Gold-Parker, T.Leijtens, B.Conings, A.Babayigit, H.G.Boyen, M.F.Toney, and M.D.McGehee, Band Gap Tuning via Lattice Contraction and Octahedral Tilting in Perovskite Materials for Photovoltaics, J.Am.Chem.Soc, 139(2017),11117-11124.

[56]S.Tiwari, G.Rathore, N.Patra, A.K.Yadav, D.Bhattacharya, S.N.Jha, C.M.Tseng, S.W. Liu, S.Biring, S.Sen, Defect mediated changes in structural, optical and photoluminescence properties of Ni substituted CeO_2, Jallcom, 782(2018), 689-698.

[57]T.Tsuboi, S. Polosan, K. Shimamura, H. Seo and M. Bettinelli, Visible and near infrared emissions of Barium-Yttrium-Fluoride crystals doped with holmium ions, The bulletin of the Research Institute of Advanced Technology Kyoto Sangyo University, 9(2010), 1-19.

[58]M.Vasile, P.Vlăzan, I.Grozescu, N.Avram, Characterization and optical properties of Er^{3+} and Ho^{3+}doped $ZnGa_2O_4$, J. Optoelectron. Adv. M , 3 (2009),1371 - 1374.

[59]F.Qin, Y.Zheng, Y.Yu, Z.Cheng, P.S.ayebi, W.Cao, Z.Zhang, Ultraviolet and violet upconversion luminescence in Ho^{3+}-doped Y_2O_3 ceramic induced by 532-nm CW laser, Jallcom, 509 (2011),1115–1118.

[60]R.Ranjan, N.Kumar, B.Behera and R.N.P.Choudhary, Investigations of electrical impedance and modulus properties of $Pb_{1-x}Sm_x$ $(Zr_{0.45}Ti_{0.55})_{1-x/4}$ O_3 ceramics, Adv.Mat.Lett, 5(2014), 138-142.

[61]K.Prasad, Lily, K. Kumari, K.P. Chandra, K.L. Yadav, S.Sen, Electrical properties of a lead-free perovskite ceramic:$(Na_{0.5}Sb_{0.5})TiO_3$, Appl.Phy.A,88(2007), 377-383.

[62]J.B.Jorcin, M.E.Orazem, N.Pebere, B.Tribollet, CPE analysis by local electrochemical impedance spectroscopy, Electrochim. Acta, 51(2006) 1473–1479.

[63]P.Thongbai, S.Tangwancharoen, T.Yamwong, S.Maensiri, Dielectric relaxation and dielectric response mechanism in (Li, Ti)-doped NiO ceramics, Phys.Condens.Matter, 20(2008), 395227.

[64]K.A.Nath, K.Prasad, K.P.Chandra, A.R.Kulkarni, Impedance and a.c. conductivity studies of $Ba(Pr_{1/2}Nb_{1/2})O_3$ ceramic, Bull.Mater.Sci, 36(2013), 591–599.

[65]G.Giovannetti, M.Aichhorn, M.Capone, Cooperative effects of Jahn-Teller distortion, magnetism, and Hund's coupling in the insulating phaseof $BaCrO_3$, Phys.Rev.B, 90(2014), 245134.

[66]R.Dhahri, M.Bejar, M.Hajlaoui, N.Sdiri, M.A.Valente, E.Dhahri, Structural properties and electrical behavior in the polycrystalline lanthanum-deficiency $La_{1\_x}\square_xMnO_3$ manganites, J.Magn.Magn.Mater, 321(2009) 1735–1738.

[67]K. Wakamura, Ion conduction in proton- and related defect (super) ionic conductors: Mechanical, electronic and structure parameters, Solid State Ion, 180(2009), 1343-1349.

[68]L.G.D.Silveira, G.S.Dias, L.F.Cotica, J.A.Eiras, D.Garcia, J.A.Sampaio, F.Yokaichiya, I.A.Santos, Charge carriers and small-polaron migration as the origin of intrinsic dielectric anomalies in multiferroic $TbMnO_3$ polycrystals, J.Phys.Condens. Matter, 25 (2013), 475401.

[69]A.Karmakar, S.Majumdar, S.Giri, Polaron relaxation and hopping conductivity in $LaMn_{1-x}Fe_xO_3$, Phys. Rev.B, 79(2009), 094406.

[70]G. La Macchia, G. Li Manni, T. K. Todorova, M. Brynda, F. Aquilante, B. O. Roos, and L. Gagliardi, On the Analysis of the Cr-Cr Multiple Bond in Several Classes of Dichromium Compounds, Inorg. Chem, (49)2010, 5216–5222.

[71]S. Nasri, A.L. Ben Hafsia, M. Tabellout, M. Megdiche, Complex impedance, dielectric properties and electrical conduction mechanism of $La_{0.5}Ba_{0.5}FeO_{3\_\delta}$ perovskite oxides, RSC.Adv, 6(2016), 76659–76665.

[72]A.R.James, K.Srinivas, Low temperature and impedance spectroscopy of PMNPT ceramics, Mat. Res. Bul, 34(1999),1301–1310.

[73]A.Rado´n, D.Łukowiec, M. Kremzer, J. Mikuła, P.Włodarczyk, Electrical Conduction Mechanism and Dielectric Properties of Spherical Shaped Fe_3O_4 Nanoparticles Synthesized by Co-Precipitation Method, Materials, 11(2018), 735.

[74]M.Tan, Y.Koseoglu, F.Alan, E.Senturk, Overlapping large polaron tunneling conductivity and giant dielectric constant in $Ni_{0.5}$ $Zn_{0.5}Fe_{1.5}Cr_{0.5}O_4$ nanoparticles (NPs), Jallcom, 509 (2011), 9399– 9405.

[75]A. Chaouchi, S. Kennour,Impedance spectroscopy studies on lead free $(Ba_{0.85}Ca_{0.15})(Ti_{0.9}$ $Zr_{0.1})O_3$ ceramics, Process.Appl.Ceram, 6(2012), 201–207.

[76]R.R.Raut, N.V.Ambhore, C.S.Ulhe, Synthesis, Structural and Dielectric Properties of La doped $95BiFeO_3$-$5BaTiO_3$ Ceramic, IJIRSET, 7(2018), 58-63.

[77]K.K.Bamzai, V.Gupta, P.N.Kotru, B.M.Wanklyn, Dielectric and A.C Conductivity Behaviour of Flux Grown Nickel Titanate ($NiTiO_3$) Crystal, Ferroelectrics, 413(2011), 328–341.

[78]J.Shanker, M.B.Suresh, D.S.Babu, Synthesis, Characterization and Impedance Spectroscopy Studies of $NdFeO_3$ Perovskite Ceramics, IJSER, 3(2015), 194-197.

[79]A.M.Azad, S.Subramaniam, Temperature dependence of the dielectric response of $BaZrO_3$ by immittance spectroscopy, Mater.Res.Bull, 37(2002), 11-22.

[80]C.Zhang, M.Shang, M.Liu, T.Zhang, L.Ge, H.Yuan, S. Feng, Multiferroicity in $SmFeO_3$ synthesized by hydrothermal method, Jallcom, 665(2016), 152-157.

[81]R.Das, K.Gupta, K.Jana, A.Nayak, U.C.Ghosh, Preparation, characterization and dielectric, ac conductivity with electrochemical behavior of strontium zirconate, Adv. Mater. Lett, 7(2016), 646-651.

[82]E.Ruff, S.Krohns, M.Lilienblum, D.Meier, M.Fiebig, P.Lunkenheimer and A.Loid, Conductivity contrast and tunneling charge transport in the vortex-like ferroelectric domain patterns of multiferroic hexagonal $YMnO_3$, Phys. Rev. Lett, 118 (2017),036803.

[83]S.K. Kar, P.Kumar, Permittivity and modulus spectroscopic study of $BaFe_{0.5}Nb_{0.5}O_3$ ceramics, Process Appl Ceram, 7(2013), 181–187.

[84]L.M.Daniels, R.J.Kashtiban, D.Kepaptsoglou, Q.M.Ramasse, J.Sloan, and R.I.Walton, Local A-Site Layering in Rare-Earth Orthochromite Perovskites by Solution Synthesis, Chem.Eur.J, 22(2016), 18362 – 18367.

[85]B.Dabrowski, J.Mais, S.Kolesnik and O.Chmaissem, Parameters controlling magnetic interactions in perovskite manganites, J.Phys.Conf.Ser, 303(2016), 012057.

[86]P.Edwards, V.Kuznetsov, D.Slocombe, R.Vijayaraghavan, The Electronic Structure and Properties of Solids, Compr. Inorg. Chem. II, 4 (2013), 153–176.

[87]M.M.El-Desoky,M.S.Ayoua, M.M.Mostafa, and M.A.Ahmed, Multiferroic Properties of Nano Structured Barium Doped Bismuth Ferrite, J.Magn.Magn.Mater, 404(2016) 68-73.

[88]S.K.Mandal, T.Rakshit, S.K.Ray, S.K. Mishra, P.S.R.Krishna and A.Chandra, Nanostructures of Sr^{2+} Doped $BiFeO_3$ Multifunctional Ceramics with Tunable Photoluminescence and Magnetic Properties, J.Phys.Condens.Matter, 25(2013), 055303.

[89]G. Dhir, P. Uniyal, and N.K. Verma, Effect of Particle Size on Multiferroism of Barium-Doped Bismuth Ferrite Nanoparticles, Mat.Sci.Semicon.Proc, 27 (2014), 611-618.

[90]R.M.Hornreich, Magnetic interactions and weak ferromagnetism in the rare-earth orthochromites, J.Magn.Magn.Mater. 7(1978), 77.

[91]J.P.Gonjal, R.Schmidt, J.J.Romero, D.Avila, U.Amador, E.Moran, Microwave-assisted synthesis, microstructure and physical properties of rare-earth chromites, Inorg.Chem, 52 (2013), 313–320.

[92]Y.Liu, H.Peng, W.Ju, H.Zhang,The Crystal Structure, Raman Spectra, and Magnetic Properties of $HoCrO_3$ Annealed in Different Atmospheres, J Supercond Nov Magn, (2018), 1-9.

[93]R.Shukla, A.K.Bera, S.M.Yusuf, S.K.Deshpande, A.K.Tyagi, W.Hermes, M.Eul and R.Pöttgen, Multifunctional Nanocrystalline CeCrO3: Antiferromagnetic, Relaxor, and Optical Properties, J. Phys.Chem.C, 113 (2009), 12663.

[94]C. Badea, R. Tetean, I.G. Deac, Suppression Of Charge And Antiferromagnetic Ordering In Ga-Doped $La_{0.4}Ca_{0.6}MnO_3$, Rom.J.Phys, 63(2018), 1-2 .

[95]R.D.McMichael, J.J.Ritter, R.D.Shull, Enhanced magnetocaloric effect in$Gd_3Ga_{5-x}Fe_xO_{12}$, J. Appl. Phys, 73(1993), 6946.

[96]A.Rostamnejadi, M.Venkatesan, P.Kameli, H.Salamati, J.M.D.Coey, Magnetocaloric effect in $La_{0.67}Sr_{0.33}MnO_3$ manganite above room temperature, J.Magn.Magne.Mater, 323(2011), 2214–2218.

[97]H. Zhang, Z.Y. Xu, X.Q. Zheng, J. Shen, F.X. Hua, J.R. Sun, B.G. Shen, Giant magnetic refrigerant capacity in Ho_3Al_2 compound, Solid State Comm. 152(2012), 1127 .

[98]L. Li, J. Wang, K. Su, D. Huo, Y. Qi, Magnetic properties and magnetocaloric effect in metamagnetic $RE_2Cu_2O_5$ (RE = Dy and Ho) cuprates, Jallcom, 658(2016), 500 .

[99]N.Panwara, S.Kumar, I.Coondoo, M.Vasundhara, N.Kumar, Low temperature magnetic and magnetocaloric studies in $YCr_{0.85}Mn_{0.15}O_3$ceramic, Physica B Condens matter, 545 (2018), 352-357.

Table 1. Space group**,** lattice parameters, tolerance factor t, unit cell volume V, orthorhombic deformation c/a, distortion bond angle O2-Cr-O1, tilt bond angle Cr-O2-Cr, average bond length Cr-O, bandwidth W, full width at half maximum fwhm, grain size D, refined fractional atomic coordinates and refinement parameters (χ^2, Bragg R-Factor, R_{wp}) at room temperature of $Ho_{1-x}Ba_xCrO_3$ and compared with other results.

Samples	HBCO0	HBCO2	HBCO3	$SmFeO_3$	$Ba_{0.7}Sb_{0.3}MnO_3$
Space groupe	Pnma	Pnma	Pnma	Pnma[30]	Pnma[31]
a(Å)	5.518_2	5.522_3	5.525_1		
b(Å)	7.534_7	7.546_9	7.556_3		
c(Å)	5.246_5	5.256_9	5.265_8		
t	0.809	0.840	0.856		
V($Å^3$)	218.089	219.012	219.794	231.85	219.4
c/a	0.950	0.952	0.953	1.424	1.353
O2-Cr-O1(°)	78.66	92.42	91.47		
Cr-O2-Cr(°)	150.6	151.12	152.05	152.38	
Cr-O(Å)	2.120	1.940	1.939		
W ~(10^{35})	0.060	0.095	0.096		
fwhm($\pm0.01\times10^{-3}$rd)	3.582	3.081	2.913		
D(±0.123nm)	40.502	47.006	49.717	100.2	49
$<R_A>$ (nm)	0.0901	0.0988	0.1032		
Ho position 4c (x,1/4,z)					
x	0.07969	0.08587	0.10217		
z	-0.01702	-0.01582	-0.01698		
Ba position 4c (x,1/4,z)					
x	0.11126	0.08587	0.10217		
z	-0.01694	-0.01582	-0.01698		
Cr position 4b (0,0,1/2)					
O1 position 4c (x,1/4,z)					
x	0.42880	0.44528	0.45980		
z	0.10448	0.09448	0.09848		
O2 position 8d (x, y, z)					
x	0.30236	0.29236	0.29229		
y	-0.15403	0.05184	0.05194		
z	0.30308	0.28736	-0.29808		
χ^2	1.133	1.331	2.041		
Bragg R-Factor	1.346	1.502	1.678		
R_{wp}	10	12	13		

Table 2. Band gap energy Eg and Urbach energy E_u values.

	HBCO0	HBCO2	HBCO3	$LaCrO_3$[53]
E_{g1}(eV)	2.305	2.188	2.080	3.09
E_{g2}(eV)	1.778	1.743	1.605	2.3
E_u (eV)	0.033	0.028	0.026	-

Table 3. Values of electrical parameters obtained from the fitting of impedance spectra.

	R_g	A_g	R_{gb}	A_{gb}	n_g	n_{gb}
HBCO0 (T=600K)	$1.176\ 10^{6}$	$7.013\ 10^{-12}$	-	-	0.997	-
HBCO2 (T=600K)	$7.380\ 10^{4}$	$4.340\ 10^{-11}$	-	-	0.928	-
HBCO3 (T=373K)	$9..30110^{7}$	$2.256\ 10^{-11}$	$1.5\ 10^{4}$	$1\ 10^{-6}$	0.964	0.96
- (T=423K)	$1.685\ 10^{7}$	$1.983\ 10^{-11}$	$1.55\ 10^{4}$	$1.102\ 10^{-6}$	0.98	0.9
- (T=473K)	$1.401\ 10^{7}$	$1.784\ 10^{-11}$	$2\ 10^{4}$	$5\ 10^{-7}$	0.988	0.89
- (T=523K)	$8.624\ 10^{6}$	$1.780\ 10^{-11}$	$4\ 10^{4}$	$6\ 10^{-8}$	0.988	0.85
- (T=573K)	$4.496\ 10^{6}$	$1.7736\ 10^{-11}$	$6.11\ 10^{4}$	$1.07\ 10^{-7}$	0.990	0.73

Table4. Activation energy values (eV)

Samples	HBCO0	HBCO2	$Ba_{0.85}\ Sb_{0.15}MnO_3$	$(Ba_{0.85}Sb_{0.15})(Ti_{0.9}Zr_{0.1})O_3$
Reference	Our work	Our work	[31]	[75]
E_a(±0.007eV)	0.518	0.452	0.494	0.743

Table5. Hopping energy and hopping distance values at several temperatures.

Samples	T(K)	W_{hop}(eV)	R_{hop} (A°)
HBCO3	373	0.67	6.128
-	423	0.742	5.938
-	473	0.807	5.775
-	523	0.870	5.631
-	573	0.932	5.504

Table 6. Comparison of dielectric constant ε', dielectric loss tanδ, relaxation dipolar time τ, AC conductivity σ_{AC} and hopping time τ_{hop} values of HBCO3 with samples of other works at 473 K and 10 KHz.

Samples	ε'($F.m^{-1}$)	tanδ	τ_1(ms)	τ_2(μs)	σ_{AC} ($\mu S.m^{-1}$)	τ_{hop} (μs)	Ref
HBCO3	85	0.7	0.9	4.6	8.8	20	Our Work
$BaZrO_3$	15	0.02	-	-	-	-	[79]
$SmCrO_3$	80	0.25	-	-	-	-	[80]
$SrZrO_3$	25	0.8	0.2	-	2	20	[81]
$YMnO_3$	150	-	10	50	1	10^{-3}	[82]

Table7. Stretched exponential parameter values at different temperature for HBCO0, HBCO2 and HBCO3 samples.

T(K)	β(HBCO0)	β(HBCO2)	β_1(HBCO3)	β_2(HBCO3)
373	-	-	0.850	0.876
473	-	-	0.862	0.883
523	-	-	0.998	0.993
673	0.735	0.776	-	-
723	0.745	0.784	-	-
873	0.769	0.813	-	-

Table 8. Magnetic ordering temperature ($T_{N,}$), maximum values of ($-\Delta S_M^{max}$) and the relative cooling power (RCP) under the magnetic field change $\mu_0\Delta H(T)$ of HBCO0, HBCO2 and HBCO3 compounds and some potential magnetic refrigerant materials.

Samples	$\mu_0\Delta H(T)$	T_N (K)	$-\Delta S_M^{max}$ ($J.Kg^{-1}.K^{-1}$)	RCP($J.Kg^{-1}$)	Reference
HBCO0	5	142	3.22	74.141	our work
HBCO2	-	142	4.59	97.172	-
HBCO3	-	143	5.79	115.479	-
$HoMnO_3$	7	12	8	152	[97]
$SmMnO_3$	5	57	7.5	75	[98]
$YCr_{0.85}Mn_{0.15}O_3$	5	39	0.186	6.65	[99]

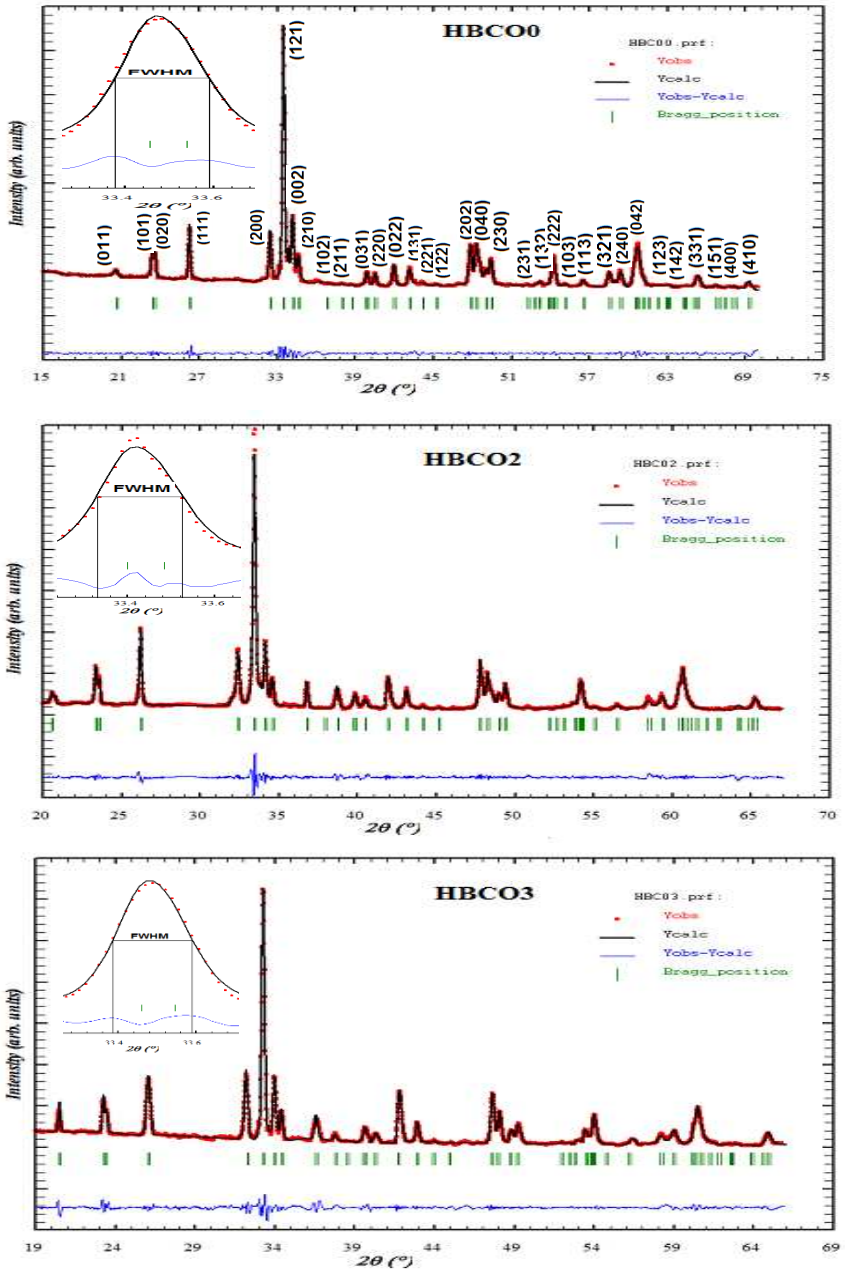

Fig 1. Rietveld fit of XRD patterns of HBCO0,HBCO2 and HBCO3 at room temperature. The red dots represent the experimental data, the continuous black curve is the calculated pattern and the blue curve at the bottom represent the difference between the experimental and calculated profiles. The green bars show the position of Bragg reflections. Insets show the fitting of the main peaks at around 2θ= 33.4°.

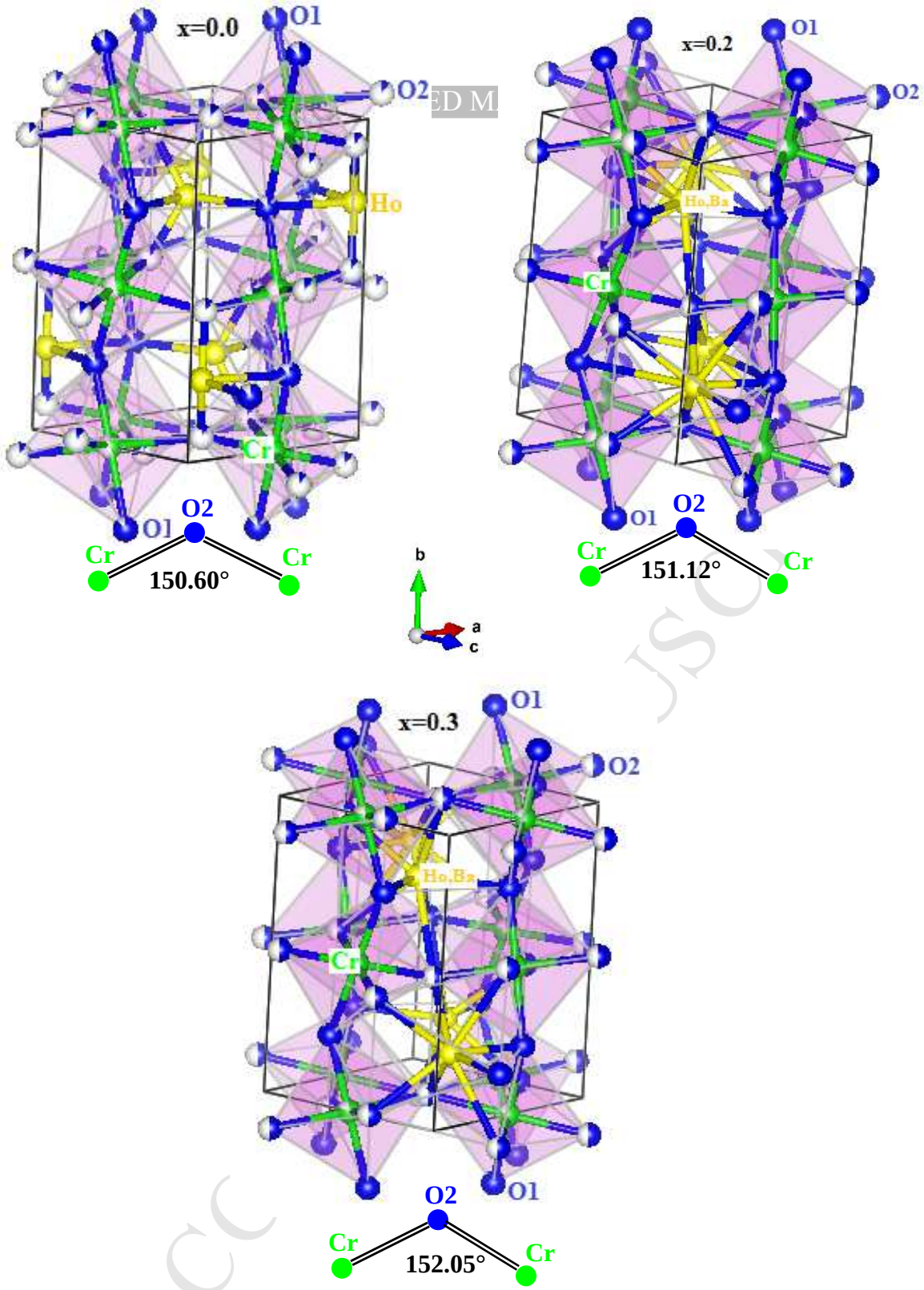

Fig 2. The graphical representation of distorted orthorhombic (Pnma) perovskite crystal structure of $Ho_{1-x}Ba_xCrO_3$ (x=0.0, 0.2, 0.3) at room temperature.

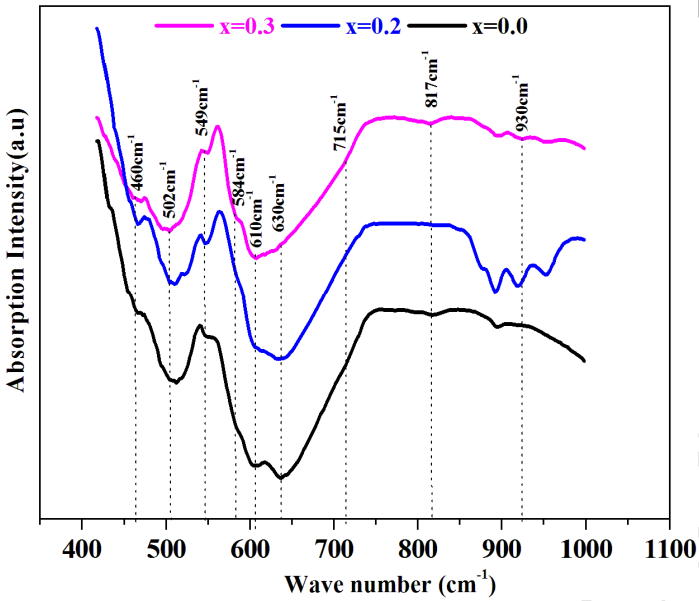

Fig. 3. IR spectra of $Ho_{1-x}Ba_xCrO_3$ (x=0.0, 0.2, 0.3) at room temperature.

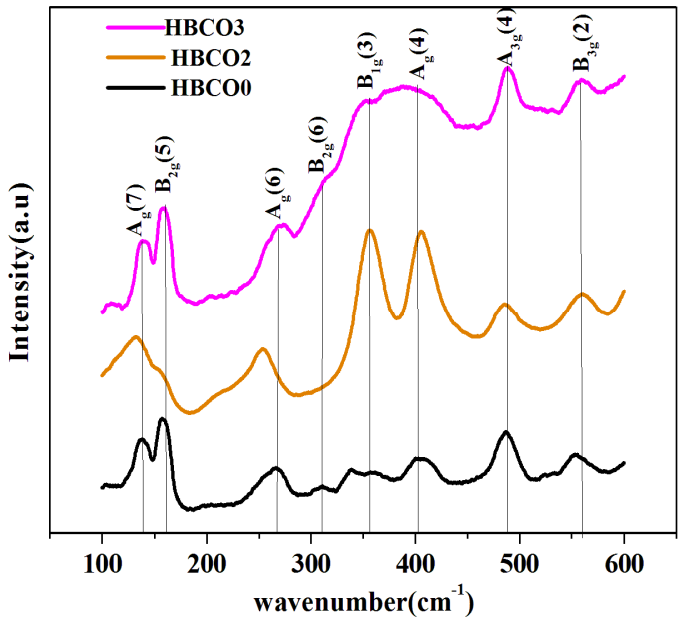

Fig 4. Raman Spectra of HBCO0, HBCO2 and HBCO3 samples at room temperature.

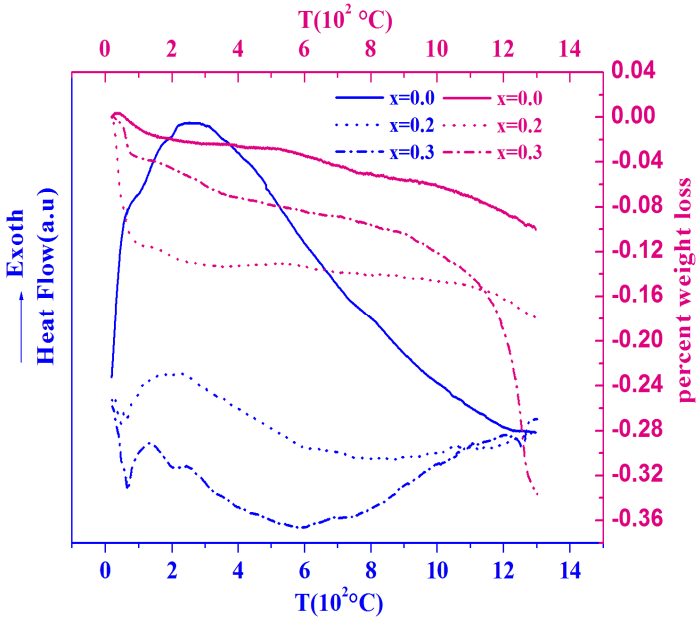

Fig 5. DTA-TGA curves of $Ho_{1-x}Ba_xCrO_3$ (x=0.0, 0.2,0.3) powder.

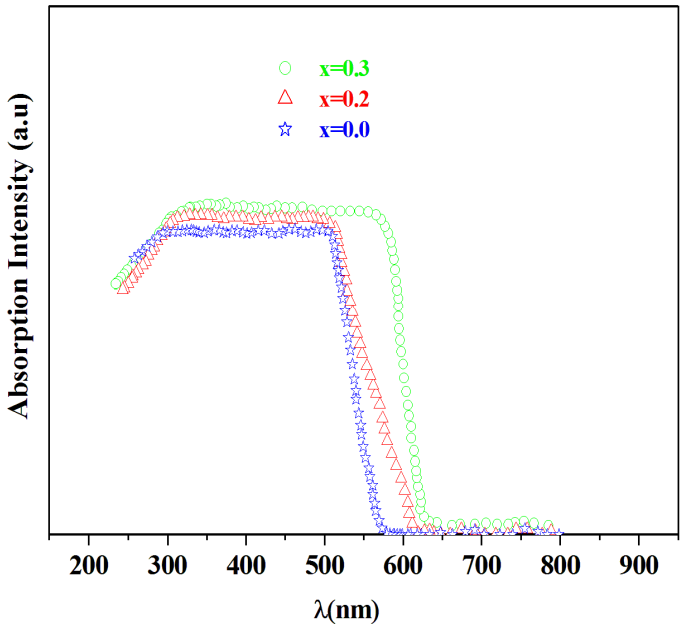

Fig 6. UV/VIS/NIR Absorption spectra of $Ho_{1-x}Ba_xCrO_3$ (x=0.0, 0.2, 0.3) powder at room temperature.

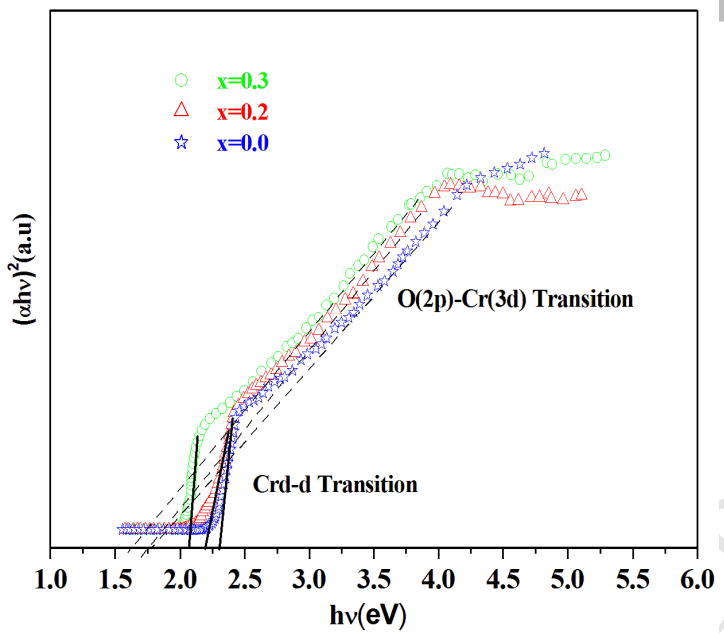

Fig 7. Plot of $(\alpha h\upsilon)^2$ vs. hυ for HBCO0, HBCO2 and HBCO3 samples at room temperature.

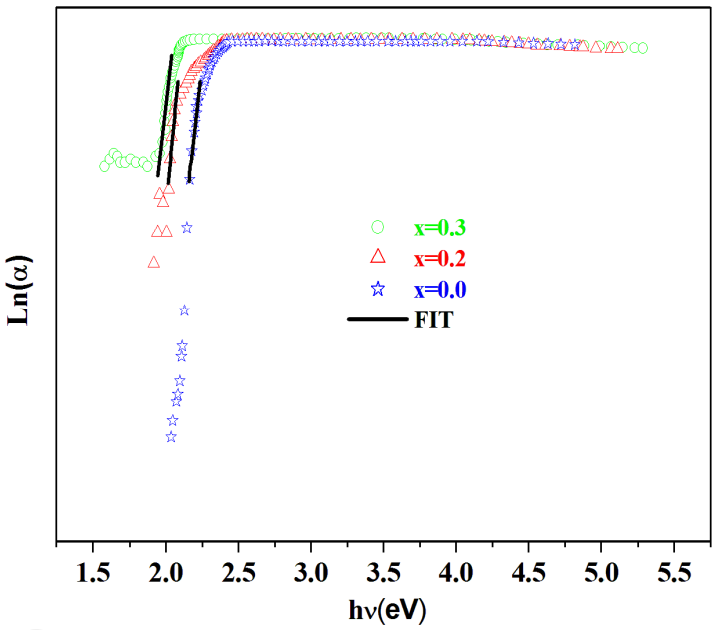

Fig 8. Ln (α) vs photon energy for HBCO0, HBCO2 and HBCO3 samples at room temperature.

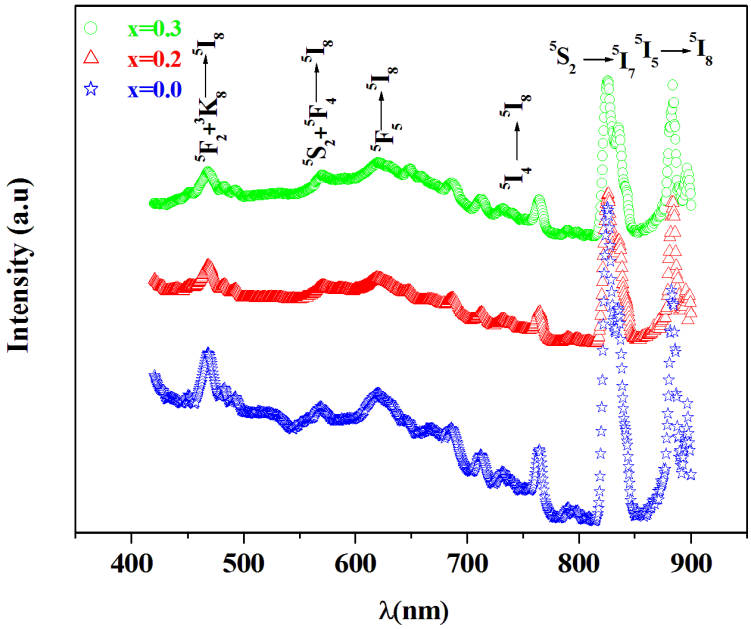

Fig 9. Emission spectra for $Ho_{1-x}Ba_xCrO_3$ (x=0.0, x=0.2 and x=0.3) powderat room temperature under the excitation wavelength λ_{ext}=280nm.

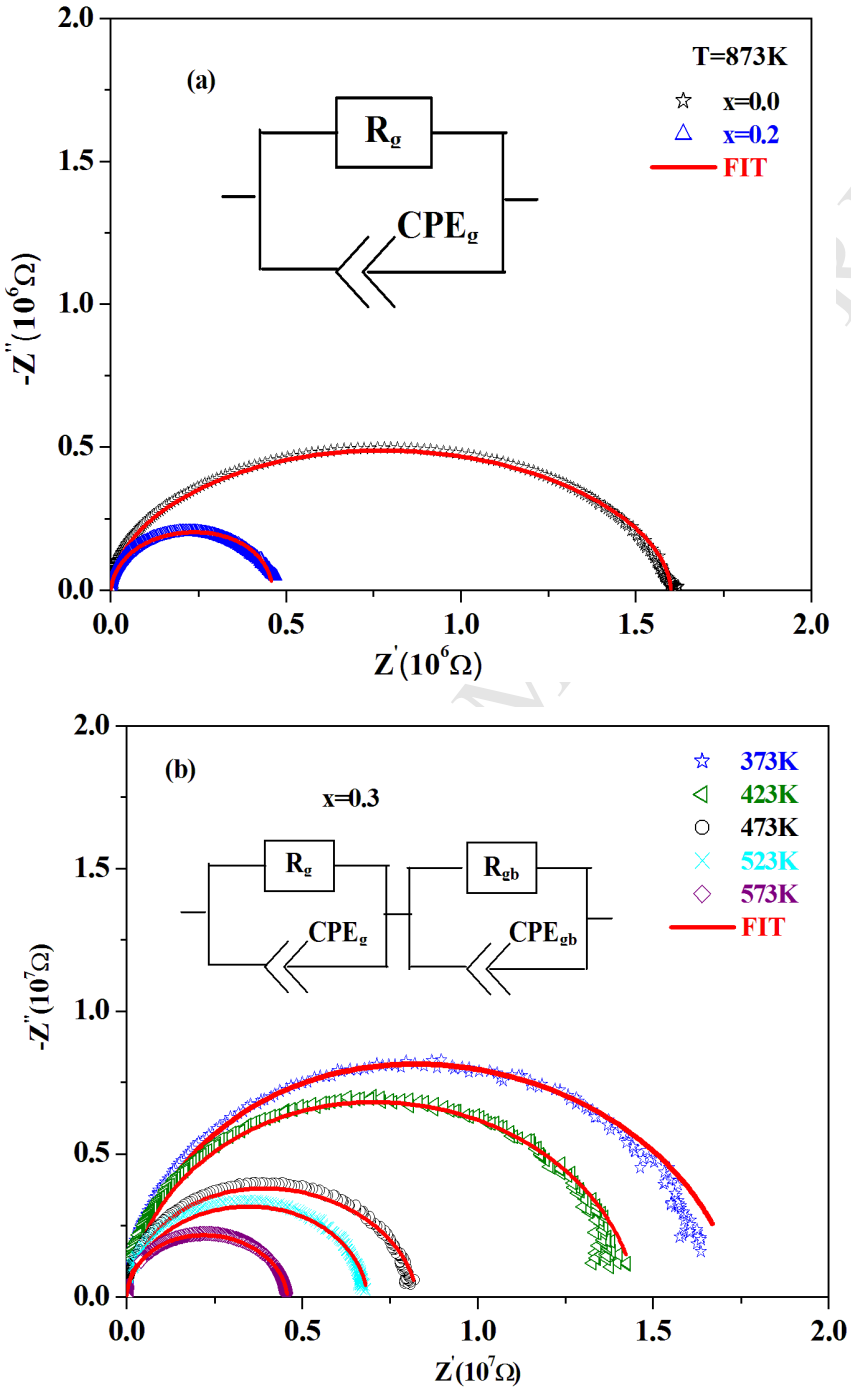

Fig 10. Nyquist (Z'-Z")plots of (a) $Ho_{1-x}Ba_xCrO_3$(x=0.0) compounds atthe temperature T=873Kand (b) Ho_{1-x} Ba_xCrO_3(x=0.3) atdifferent temperatures with electrical equivalent circuits (inset).

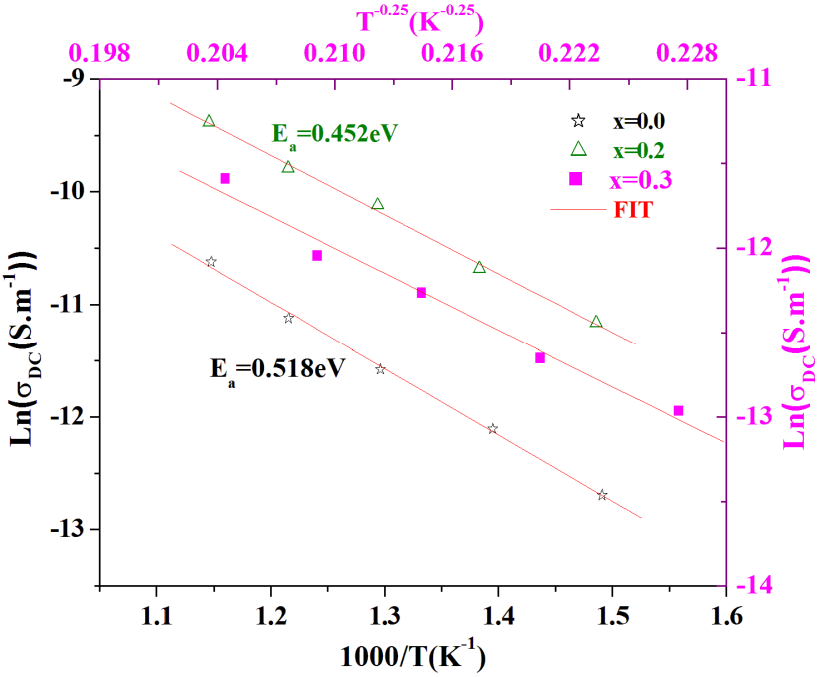

Fig 11. Temperature dependence of Ln(σ_{DC}) HBCO0, HBCO2 and HBCO3 samples.

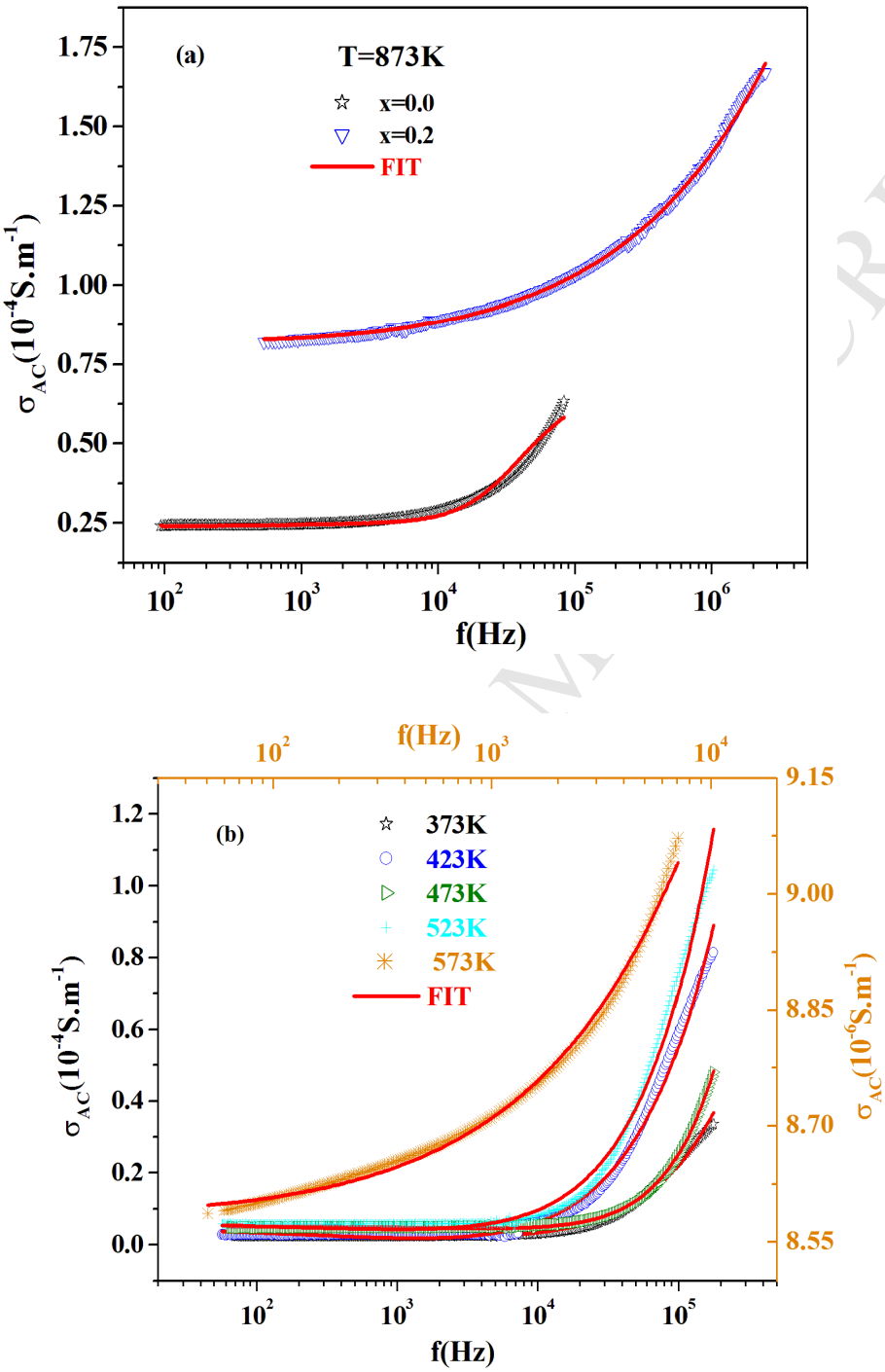

Fig12. Frequency dependence of the AC conductivity (σ_{AC}) for (a) Ho_{1-x} Ba_xCrO_3(x=0.0, x=0.2) compounds at the temperature T=873Kand (b) for Ho_{1-x} Ba_xCrO_3(x=0.3) at different temperatures.

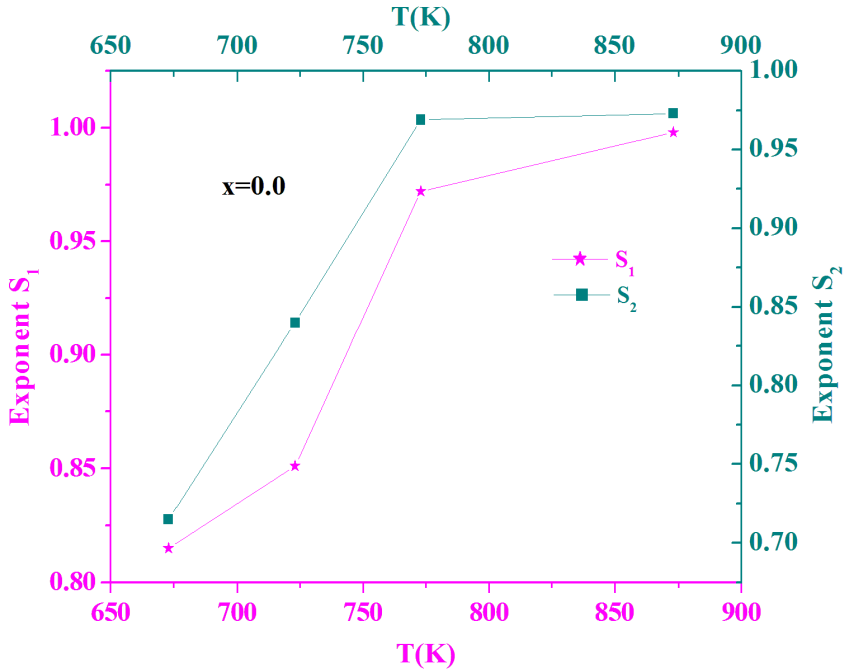
T(K)
650
700
750
800
850
900
1.00
0.95
0.90
0.85
0.80
Exponent S1
Exponent S2
0.75
0.70
x=0.0
S1
S2

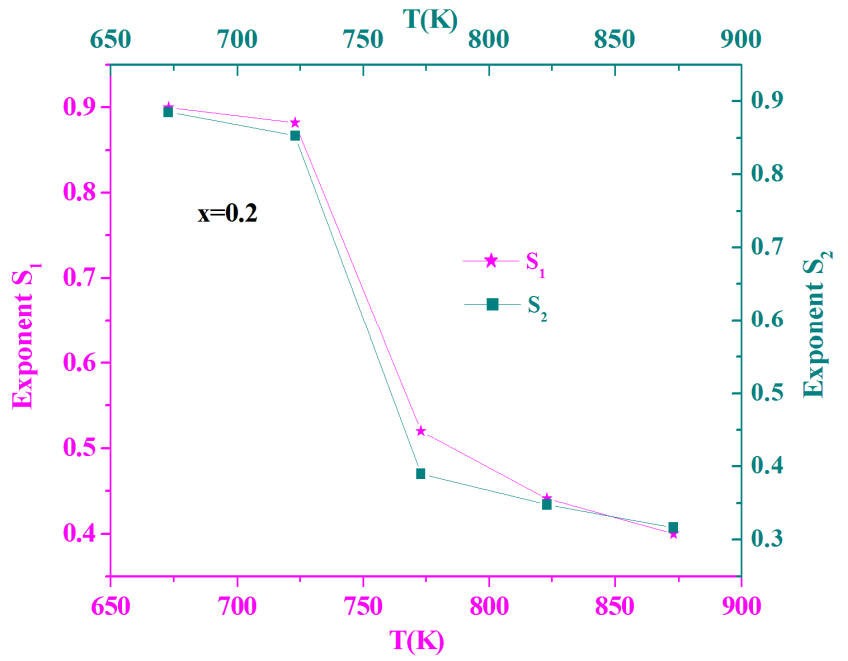
T(K)
650
700
750
800
850
900
0.9
0.8
0.7
0.6
0.5
0.4
0.3
Exponent S1
Exponent S2
x=0.2
S1
S2

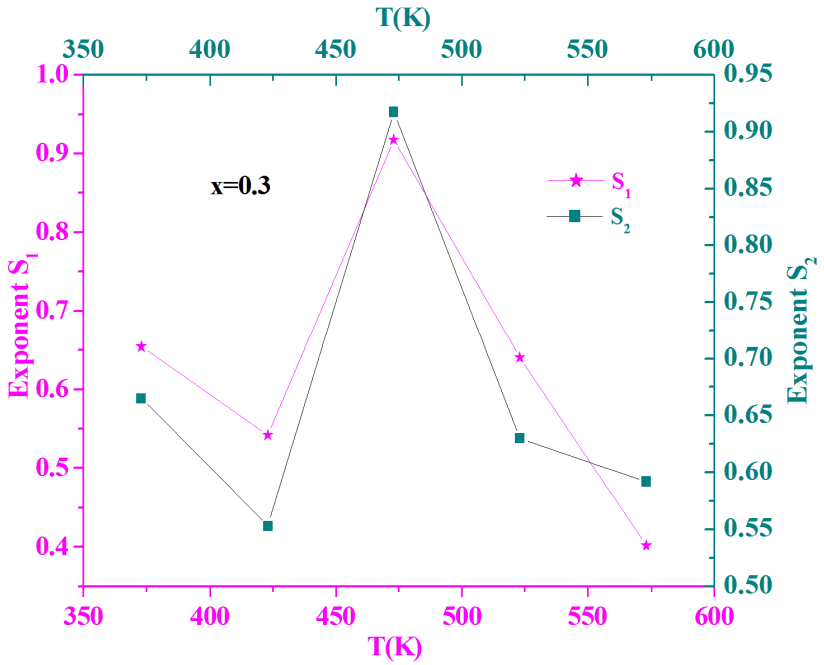

Fig13. Temperature dependence of the exponent S for Ho_{1-x} Ba_xCrO_3(x=0.0, 0.2 and 0.3).

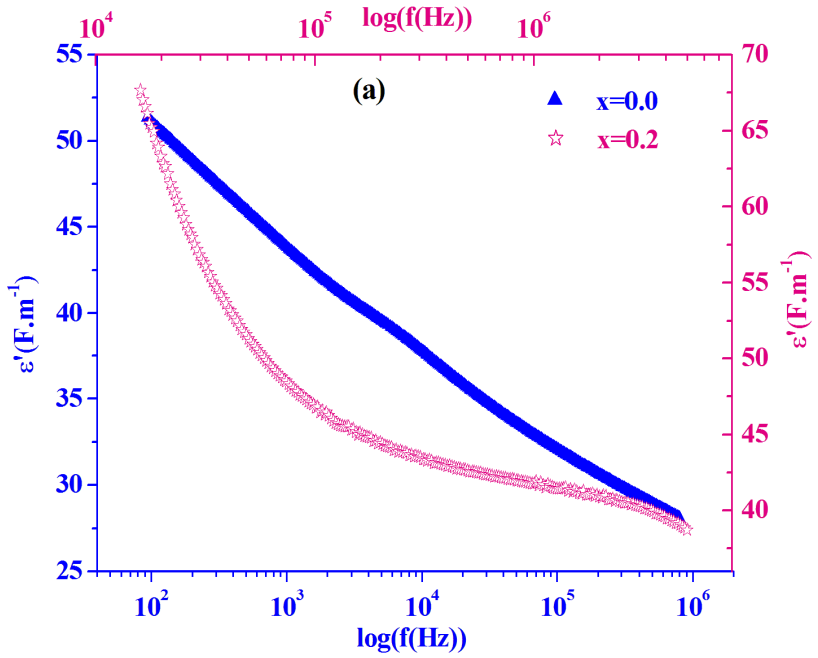

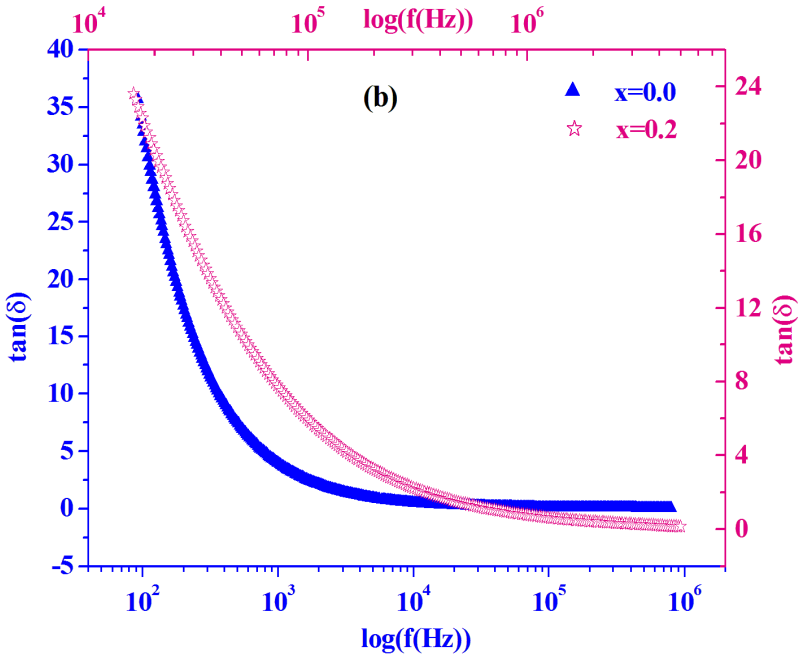

Fig 14. (a)Frequency dependence of the dielectric constant (ε') and (b) the dielectric loss (tanδ) for Ho_{1-x} Ba_xCrO_3(x=0.0, x=0.2) compounds at the temperature T=773K.

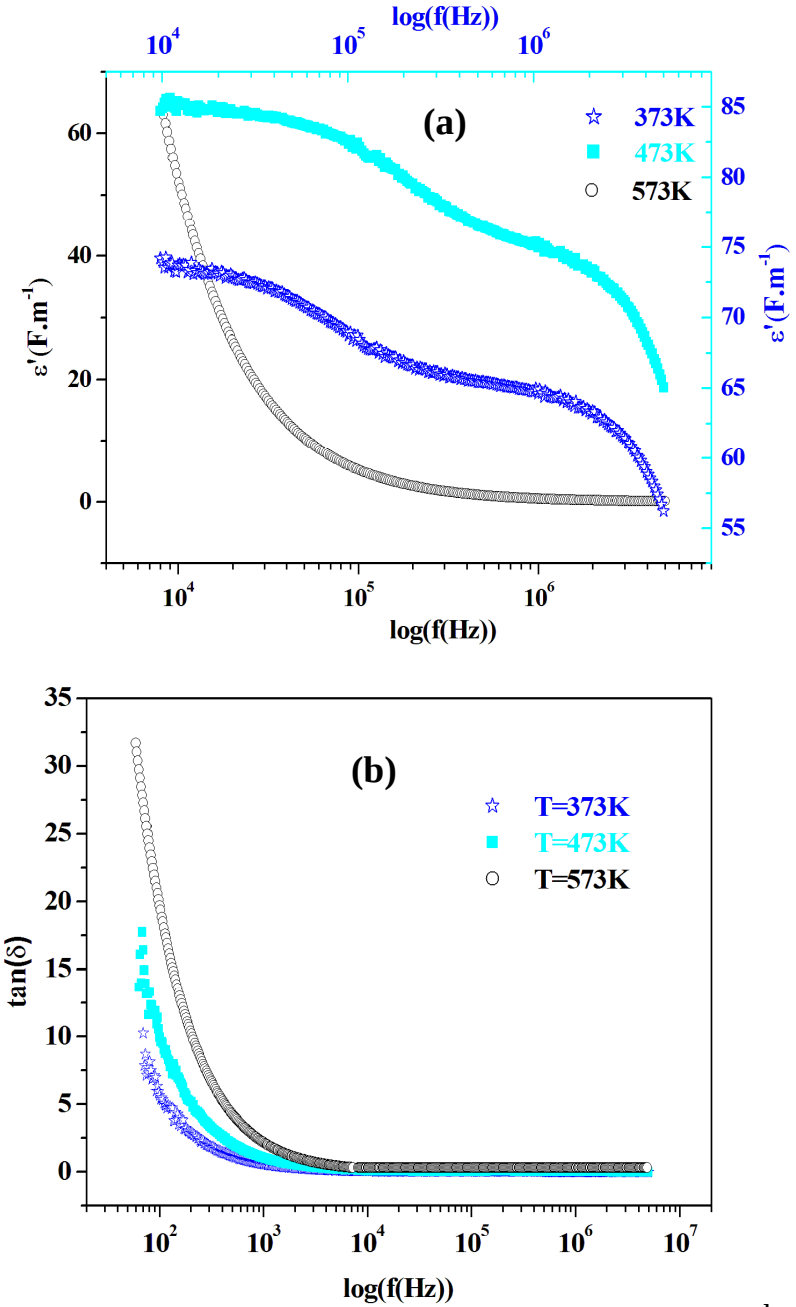

Fig 15.(a) Frequency dependence of the dielectric constant (ε') and (b) the dielectric loss (tanδ)for $Ho_{1-x}Ba_xCrO_3$(x=0.3) at different temperatures.

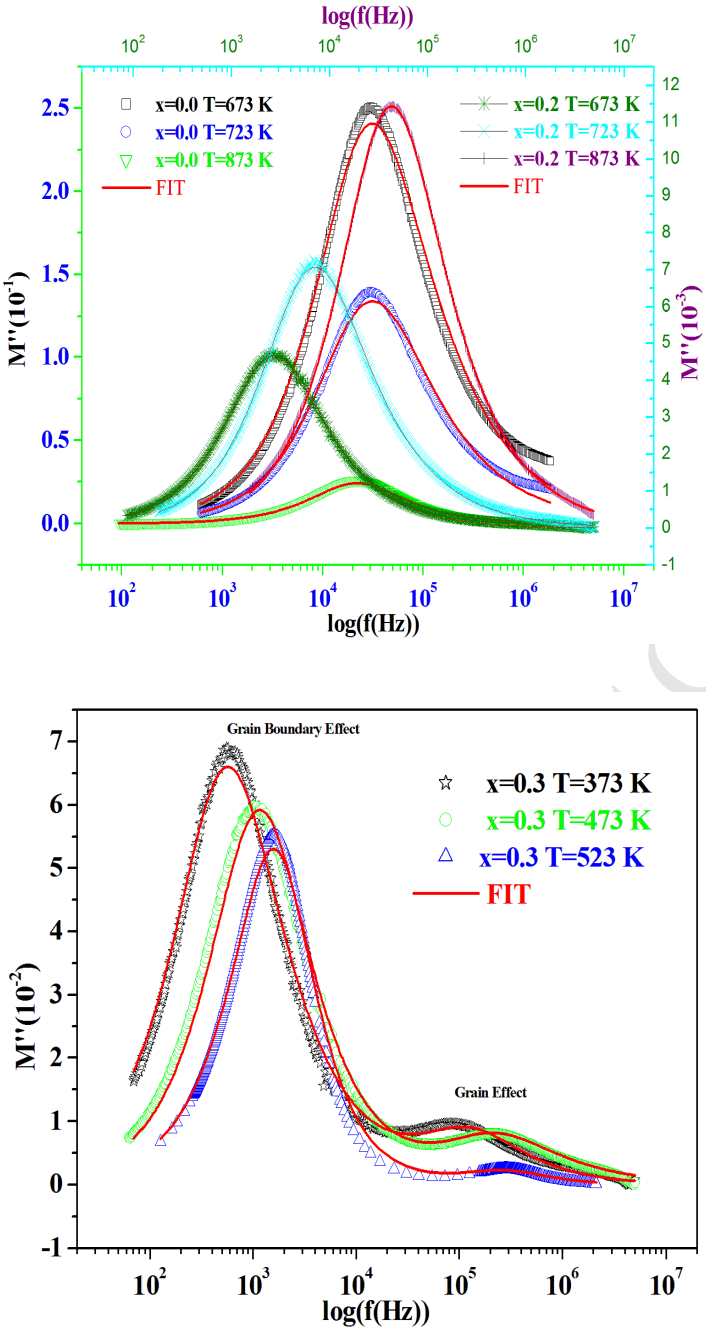

Fig 16. Frequency dependence of the electric modulus (imaginary part M") for (a) HBCO0, HBCO2 and (b) HBCO3 samples.

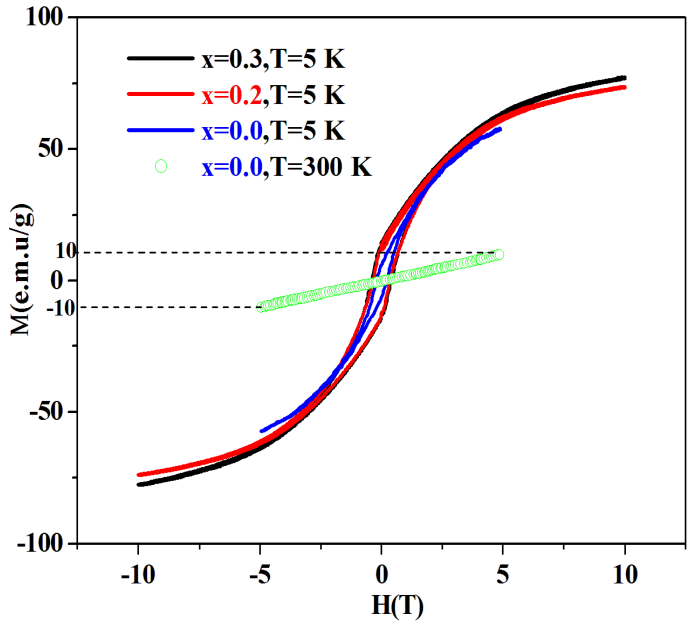

Fig 17. Hysteresis curves measured at T=5K for Ho_{1-x} Ba_xCrO_3(x=0.0, 0.2 and 0.3) and for$HoCrO_3$ at 300K.

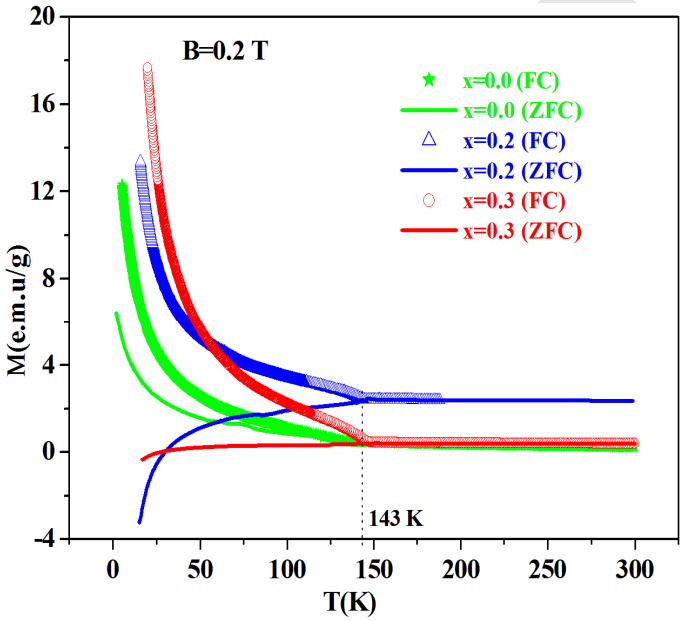

Fig 18. Temperature dependence of magnetization for $Ho1_{-x}$ Ba_xCrO_3(x=0.0, 0.2 and 0.3) measured at 0.2T.

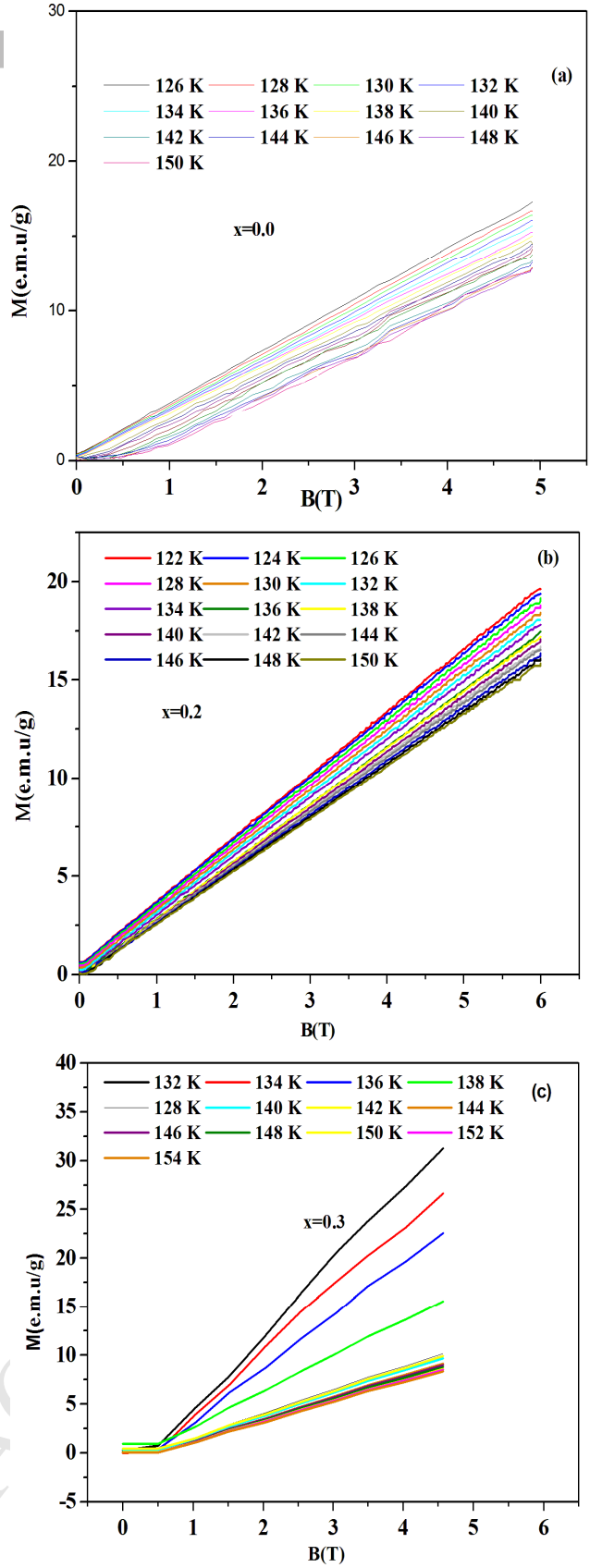

Fig 19. Magnetization vs. applied magnetic field, measured at different temperatures, for HBCO0, HBCO2 and HBCO3 samples.

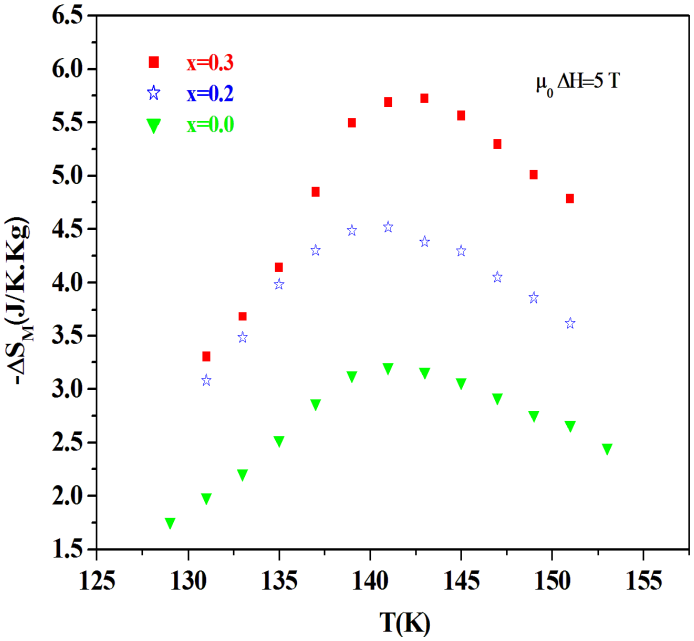

Fig 20. Temperature dependence of the magnetic entropy change ΔS_M upon the field change of 5 T for HBCO0, HBCO2 and HBCO3 samples.

.